



Single-cell mtDNA dynamics in tumors is driven by coregulation of nuclear and mitochondrial genomes

Received: 21 June 2022

Accepted: 20 March 2024

Published online: 13 May 2024

Check for updates

Minsoo Kim^{1,2}, Alexander N. Gorelick^{1,2,3}, Ignacio Vázquez-García^{1,2}, Marc J. Williams^{1,2}, Sohrab Salehi², Hongyu Shi², Adam C. Weiner^{1,2}, Nick Ceglia², Tyler Funnell^{1,2}, Tricia Park^{1,2}, Sonia Boscenco², Ciara H. O'Flanagan⁴, Hui Jiang^{1,3}, Diljot Grewal², Cerise Tang², Nicole Rusk^{1,2}, Payam A. Gammage^{1,5,6}, Andrew McPherson², Sam Aparicio^{1,4}, Sohrab P. Shah^{1,2}✉ & Ed Reznik^{1,2}✉

The extent of cell-to-cell variation in tumor mitochondrial DNA (mtDNA) copy number and genotype, and the phenotypic and evolutionary consequences of such variation, are poorly characterized. Here we use amplification-free single-cell whole-genome sequencing (Direct Library Prep (DLP+)) to simultaneously assay mtDNA copy number and nuclear DNA (nuDNA) in 72,275 single cells derived from immortalized cell lines, patient-derived xenografts and primary human tumors. Cells typically contained thousands of mtDNA copies, but variation in mtDNA copy number was extensive and strongly associated with cell size. Pervasive whole-genome doubling events in nuDNA associated with stoichiometrically balanced adaptations in mtDNA copy number, implying that mtDNA-to-nuDNA ratio, rather than mtDNA copy number itself, mediated downstream phenotypes. Finally, multimodal analysis of DLP+ and single-cell RNA sequencing identified both somatic loss-of-function and germline noncoding variants in mtDNA linked to heteroplasmy-dependent changes in mtDNA copy number and mitochondrial transcription, revealing phenotypic adaptations to disrupted nuclear/mitochondrial balance.

Tumors commonly accumulate mutations and copy number alterations to mitochondrial DNA (mtDNA)^{1,2}. The functional effects of these genetic changes on cell metabolism^{3,4}, apoptotic potential^{5,6}, innate immunity⁷ and other phenotypes depend on at least the following two key factors: the fraction of mutated mitochondrial genomes in the cell (heteroplasmy) and the total number of mtDNAs in the cell (mtDNA copy number)^{8,9}. Furthermore, because mtDNA mutations normally arise over the course of human development, somatic cell

division, aging and tumorigenesis, mtDNA genotypes are nonrandomly distributed across cells and consequently display potentially large cell-to-cell variation^{2,10,11}.

The prevalence of intracellular and intercellular variability in mtDNA genotype represents both a critical confounder to the characterization of phenotypes associated with mtDNA mutations and an effective cell-endogenous mutational barcode for tracing ongoing somatic evolution¹². To date, several techniques such as single-cell

¹Tri-Institutional PhD Program in Computational Biology & Medicine, Weill Cornell Medicine, New York City, NY, USA. ²Computational Oncology, Department of Epidemiology and Biostatistics, Memorial Sloan Kettering Cancer Center, New York City, NY, USA. ³Human Oncology and Pathogenesis Program, Memorial Sloan Kettering Cancer Center, New York City, NY, USA. ⁴Department of Molecular Oncology, British Columbia Cancer Research Centre, Vancouver, British Columbia, Canada. ⁵Institute of Cancer Sciences, University of Glasgow, Glasgow, UK. ⁶CRUK Beatson Institute, Glasgow, UK. ✉e-mail: shahs3@mskcc.org; reznike@mskcc.org

RNA sequencing (scRNA-seq) and single-cell transposase-accessible chromatin sequencing (scATAC-seq) have been applied to measure mtDNA genotypes across tumors, focusing exclusively on the detection of somatic mutations (as opposed to mtDNA copy number) for use as cell-endogenous lineage markers^{13–16}. These methods typically require DNA amplification or other approaches to library preparation that inhibit accurate quantification of the absolute mtDNA copy number in a single cell. Yet, the total number of wild-type mtDNA copies, which is determined jointly by heteroplasmy and the total mtDNA copy number, is a key property for understanding the genotype-phenotype map of pathogenic mtDNA mutations^{8,17,18}. A comprehensive understanding of mtDNA genotypic variability, evolution and functional consequences therefore requires joint measurement of genotype and absolute copy number.

We previously developed a single-cell whole-genome sequencing (scWGS) platform called Direct Library Prep (DLP+) to study genome plasticity, cell-to-cell variation and clonal evolution driven by copy number alterations of the nuclear genomes of human cancers and model systems^{19–21}. Because DLP+ is amplification-free and mtDNAs exist in multiple copies within each cell, it uniquely enables the simultaneous, high-fidelity interrogation of mtDNA genotype, mtDNA copy number and nuclear DNA (nuDNA) genotype across single cells. Here we analyzed DLP+ data of 72,275 single cells from engineered breast epithelial cell lines, patient-derived xenograft models of triple-negative breast cancer (TNBC) and high-grade serous ovarian cancer (HGSC) and primary HGSC tumors. Through the application of computational methods to this unique collection of single-cell genomes, we interrogated the regulatory architecture that quantitatively connects single-cell variation in mitochondrial and nuclear genotypes to downstream phenotypes.

Results

Per-cell mtDNA copy number quantification by DLP+

To study mtDNA copy number and heteroplasmy jointly at single-cell resolution, we collected scWGS (DLP+) libraries from a variety of distinct biological settings covering nontransformed cell lines, patient-derived xenografts (PDXs) and primary human tumors (Fig. 1a,b and Supplementary Table 1). These data included previously published^{19–21} sequencing of cell lines from (1) GM18507 diploid lymphoblastoid cell line ($n = 3,203$ cells), (2) nontransformed 184-hTERT mammary epithelial cell line ($n = 4,011$ cells), (3) four *TP53^{-/-}*;184-hTERT cell lines ($n = 30,012$ cells), (4) engineered *TP53^{-/-}*;*BRCA2^{+/+}*;184-hTERT cell line ($n = 2,012$ cells), (5) two *TP53^{-/-}*;*BRCA2^{+/+}*;184-hTERT cell lines ($n = 1,056$ cells), (6) *TP53^{-/-}*;*BRCA1^{+/+}*;184-hTERT cell line ($n = 463$ cells) and (7) *TP53^{-/-}*;*BRCA1^{+/+}*;184-hTERT cell line ($n = 430$ cells), as well as the ovarian cancer cell line OV2295 ($n = 573$ cells), cervical cancer cell line HeLa ($n = 507$ cells) and HER2+ breast cancer cell line T-47D ($n = 2,534$ cells). Furthermore, our dataset included 12 different PDX models of TNBC ($n = 23,466$ cells), three of which were cisplatin-treated ($n = 7,300$ cells), one HGSC PDX ($n = 38$ cells) and five primary HGSC tumors ($n = 4,150$ cells) including two newly sequenced surgical resections for a total of 32 distinct samples. For 18 of these samples (eight cell line samples, seven PDX samples and three primary tumor samples), matching scRNA-seq from the same sample was available. Many samples include multiple sequencing libraries performed at different time points as part of a serial passaging experiment, resulting in 127 distinct libraries (median 507 cells per library).

We first compared the coverage of mtDNA in DLP+ and matching 3'-enriched 10× scRNA-seq. Reads aligning to mtDNA were abundant across all cells and, in contrast to the scRNA-seq, covered the entire mitochondrial genome (Fig. 1c). In total, 93.96% of the mitochondrial genome had higher coverage in DLP+ compared to scRNA-seq, enabling comparatively robust mtDNA variant calling and mtDNA copy number estimation directly from primary DLP+ sequencing data. Read depth per cell and the relative capture efficiency of mtDNA/nuDNA

had a low correlation, suggesting minimal technical bias derived from sequencing depth in calculating mtDNA copy number ($R = 0.03$, $P < 10^{-15}$; Extended Data Fig. 1a). Notably, DLP+ data were both broader and deeper compared to scRNA-seq data from the same sample in seven PDX (Kolmogorov-Smirnov test, all $P < 2.2 \times 10^{-16}$; Fig. 1d,e).

Unlike most other single-cell DNA sequencing technologies, DLP+ does not use pre-amplification, enabling relatively unbiased quantification of both nuclear and mtDNA copy numbers at single-cell resolution. Following prior work^{2,22}, we estimated mtDNA copy number by comparing the read depth of mtDNA- and nuDNA-aligned reads and calibrating mtDNA ploidy to the baseline ploidy of nuDNA. Lymphoblastoid GM18507 cells typically contained 756 copies of mtDNA per cell (25th and 75th percentiles: 575 and 999, respectively) with highly robust and reproducible mtDNA copy number estimates across sequencing libraries (Extended Data Fig. 1b). In silico downsampling of one of the libraries deeply sequenced with a median mtDNA read depth of 79× per cell to a median mtDNA read depth of 8× per cell indicated stable estimation of mtDNA copy number and heteroplasmic mtDNA variant calling down to 30% of the original sequencing depth (Extended Data Fig. 1c–g). The presence of ~1,000 copies of mtDNA per cell is consistent with lower-throughput digital droplet polymerase chain reaction estimates of single-cell mtDNA copy number²³. Together with the reproducibility of such estimates across sequencing libraries, these analyses establish DLP+ as a robust high-throughput assay for single-cell mtDNA copy number quantification.

mtDNA copy number correlates with cell size

We analyzed DLP+ sequencing data of treatment-naive samples along with 3,203 GM18507 diploid lymphoblastoid cells, included in several DLP+ runs as controls for nuDNA copy number estimation, for a total of 55,930 cells (Methods; Supplementary Table 1). Median copy number across these diverse cells varied from 531 in the TNBC PDX model SA1142 to 3,274 in the *BRCA1^{-/-}*;*TP53^{-/-}*;184-hTERT cell line sample SA1054 (Fig. 2a). Per-cell mtDNA copy number estimates were reproducible across technical replicates and exhibited a high degree of temporal stability across multiple 184-hTERT cell lines (Fig. 2b–d and Extended Data Fig. 2a). In contrast to population-level stability in mtDNA copy number, cell-to-cell variation in any single library was substantial (Fig. 2a). Most libraries exhibited a typical coefficient of variation of 0.65, consistent with observations in embryos and parathyroid^{24,25} and the per-sample variation observed in Pan-Cancer Analysis of Whole Genomes (PCAWG) bulk whole genomes of the corresponding cancer type² (Extended Data Fig. 2b).

Next, we used mtDNA copy number quantification from DLP+ to interrogate cell-type-specific mtDNA copy number levels in both malignant and nonmalignant cells from the tumor microenvironment. Prior analysis of mtDNA copy number levels in tumors has focused on comparing estimates of mtDNA copy number from bulk tumor sequencing to matched adjacent-normal tissue¹, potentially conflating changes in cellular composition with tumor-cell-intrinsic adaptations in mtDNA copy number. In four primary HGSC tumors with DLP+, we were able to identify both malignant and nonmalignant (corresponding to a mixture of stromal and immune) cells on the basis of nuDNA copy number profiles and found that malignant cells displayed a significantly higher mtDNA copy number ($\log_2(\text{fold change}) = 1.3\text{--}3.0$; all $P < 10^{-14}$; Extended Data Fig. 2c). These data indicate that mtDNA copy number is elevated in tumor cells relative to colocalized nontumor cells in TNBC and HGSC. Further conclusions from this analysis, however, are limited by the inability to definitively distinguish nontransformed cells of a common cell-of-origin to HGSC from other nontransformed cells such as immune cells.

As mitochondria provide anabolic substrates for both cellular maintenance and proliferation^{26–29}, we hypothesized that cell-to-cell

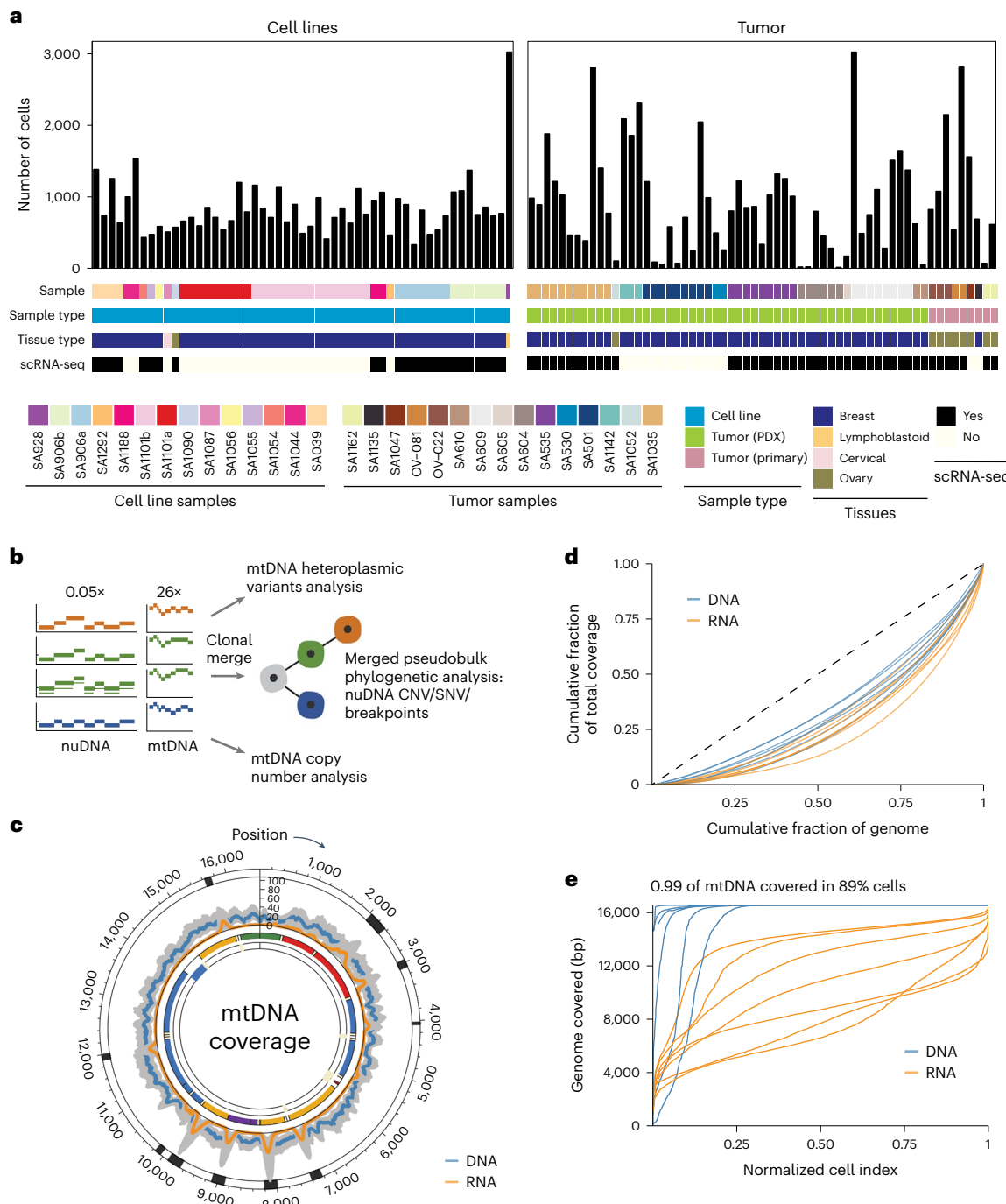


Fig. 1 | Overview of the data and coverage information. **a**, Summary of the data with histogram indicating the number of cells per DLP+ library corresponding to the samples, annotated by the data type and tissue type. **b**, Schematic representation of DLP+ showing the ability to capture both mtDNA sequence for heteroplasmic variant analysis and absolute mtDNA copy number, along with phylogenetic analysis based on the nuclear genome copy number profile. **c**, Circos plot of the median read coverage across all the samples on a linear scale with the upper and lower bands representing the first and third quartiles.

Coverage for DLP+ is in blue, and coverage for scRNA-seq is in orange. The outer track indicates the regions where the coverage breadth is higher in 3'-end scRNA-seq than in DLP+. The mtDNA genes are annotated and colored by mitochondrial complexes. **d**, Lorenz curve with cumulative proportion of total genome coverage on the y-axis and the cumulative proportion of bases on the x-axis. Each curve for DLP+ and 10× scRNA-seq was plotted using the seven PDX genomes. **e**, Depth-of-coverage curves for DLP+ and 10× scRNA-seq for the same seven PDX genomes.

variation in mtDNA copy number within clonally related cells may reflect bona fide variation in the energetic and anabolic demands of single cells^{30,31}. Such changes in anabolic demand might, for example, result from normal variation in cell size, which has been previously posited in the literature and recently quantified in budding yeast^{24,25,32}. We analyzed coregistered bright field images from the DLP+ platform ($n = 4,011$ 184-hTERT breast epithelial cells, $n = 26,024$ of eight

184-hTERT-derived cell lines and $n = 1,731$ GM18507 diploid lymphoblastoid cells) and correlated estimates of cell size from these images with single-cell mtDNA copy number. The diameter of diploid cells ranged from 10.43 μm to 50.38 μm and varied significantly according to lineage (Extended Data Fig. 2d). This corresponded to an approximate 24 and 29.2 mtDNA copy number increase per micron, respectively (Extended Data Fig. 2e). In total, 46/52 sequencing libraries (covering

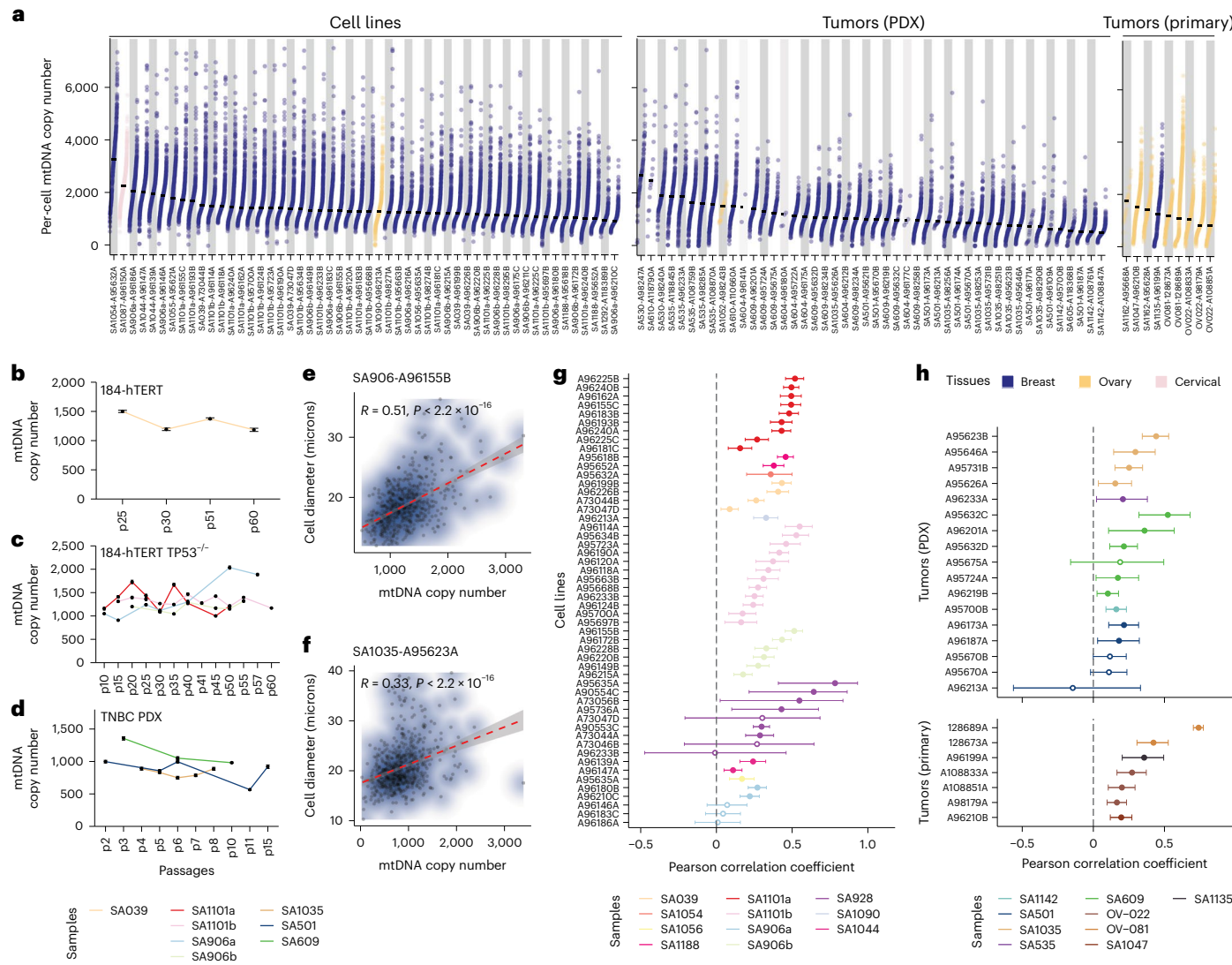


Fig. 2 | Relative increase in mtDNA copy number with larger cell size.

11 distinct cell lines) demonstrated a statistically significant positive correlation between cell size and mtDNA copy number (Pearson correlation, $Q < 0.05$; Fig. 2e,g), corroborating previous studies in budding yeast^{27,32,33}. We then studied tumor cells, analyzing 5,476 images of cells across 40 libraries of six TNBC PDX models and 4,005 images across nine libraries of five primary HGSC samples. In total, 20/24 sequencing libraries showed a significant positive correlation between cell diameter and mtDNA copy number (Fig. 2f,h). We also correlated the mtDNA-to-nuDNA ratio (MNR), that is, the number of copies of mtDNA per average haploid nuclear genome, against cell diameter, and found statistically significant results across conditions (Extended

p11 and p15 ($n = 2,153$ cells). e, Scatter plot showing a positive Pearson correlation ($R = 0.51, P = 1.54 \times 10^{-43}$) between mtDNA copy number and cell diameter for a sequencing library of a *TP53*^{-/-} 184-hTERT SA906b cell line, A96155B ($n = 627$ cells). Contours represent a two-dimensional kernel density estimate. Gray-shaded areas represent error bands indicating the 95% confidence interval, and the red dashed line indicates the regression line. f, Same as e but for a Pearson correlation ($R = 0.33, P = 1.16 \times 10^{-19}$) on a sequencing library of a TNBC SA1035 PDX, A95623A ($n = 704$ cells). g, Dot-and-whisker plot of the Pearson correlation coefficient for every library across all the cell lines ($n = 52$). Consistent, positive coefficient estimation across multiple libraries of the same sample corroborates the relationship between cell size and mtDNA copy number. The dots have their colors filled in only if the library is statistically significant (false discovery rate (FDR) < 0.05). Error bars indicate 95% confidence intervals. h, Same as g but for tumors ($n = 17$ and 7 libraries for PDXes and tumors, respectively).

Data Fig. 2f,g). These findings confirm that, in both cultured cells and human tumors, cell-to-cell variation in mtDNA copy number is associated with a biophysical adaptation in cell size.

Stoichiometric adaptation of mtDNA copy number to whole-genome doubling (WGD)

We hypothesized that somatic alterations in the nuclear genome, and especially large-scale changes to total copy number might contribute to the extensive variation in mtDNA copy number observed in Fig. 2a. In particular, we anticipated that WGD events, which have previously been associated with large metabolic changes and increase

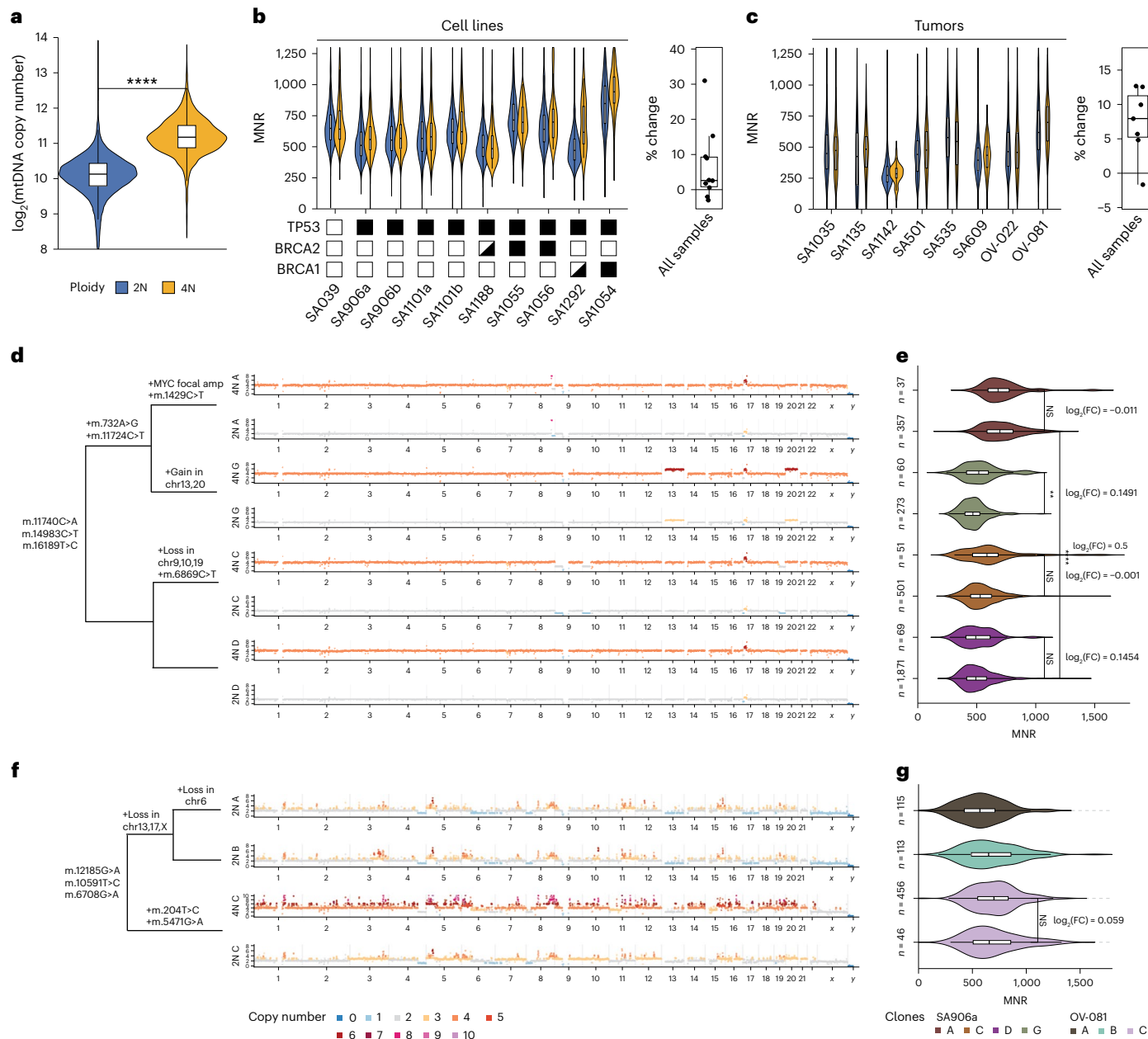


Fig. 3 | MNR homeostatically balances with WGD but exhibits clone-specific differences. **a**, Distribution of per-cell mtDNA copy number of all the diploid ($n = 42,351$) and tetraploid ($n = 6,269$) cells, colored by nuDNA ploidy. Two-sided, two-sample Wilcoxon test indicates that diploid cells have a significantly different mtDNA copy number compared to tetraploid cells ($P < 10^{-16}$). Boxplots represent the median, 25th percentile and 75th percentile, and whiskers correspond to 1.5 times the interquartile range. **** denotes $P \leq 0.0001$. **b**, Left, violin plots of per-cell MNR between diploid and tetraploid cells of all the cell lines derived from 184-hTERT breast epithelial cells ($n = 10$ samples). Filled and half-filled boxes indicate homozygous and heterozygous loss-of-function genotypes, respectively. Right, boxplot showing the distribution of percent change in MNR from diploid to tetraploid cells. All boxplots represent the median, 25th percentile and 75th percentile, and whiskers correspond to 1.5 times the interquartile range. Bottom, the haplotype-specific states. **c**, Same as **b** but for PDX models and primary tumor samples ($n = 8$ samples). **d**, nuDNA

copy number profile of *TP53*^{-/-} 184-hTERT cell line SA906a for diploid and tetraploid cells of clones A, C, D and G ($n = 3,219$ cells). Colors correspond to copy number states. A phylogenetic tree with major mutational events in both genomes labeled on the left. amp, amplification. **e**, Violin plots of MNR for each of the clones, split into diploid and tetraploid cells. Diploid and tetraploid cells of clones A, C and D indicate NS differences in MNR (two-sided Wilcoxon test). Clone G shows a significant difference (two-sided Wilcoxon test), but the FC is small. All boxplots represent the median, 25th percentile and 75th percentile, and whiskers correspond to 1.5 times the interquartile range. ** denotes $P < 0.001$ and **** denotes $P \leq 0.0001$. **f**, Same as **d** but for clones A, B and C in a primary HGSC sample, SPECTRUM-OV-081 ($n = 730$ cells). Clone C has both diploid and tetraploid cells. **g**, Same as **e** but for a primary HGSC sample, SPECTRUM-OV-081. There is no significant difference in the MNR of diploid and tetraploid cells of clone C (two-sided Wilcoxon test). NS, not significant; FC, fold change.

in cell sizes and are common in TNBC and HGSC, may be major contributors to mtDNA copy number variation in any given sample^{34,35}. WGD was a readily identifiable and frequent event in DLP+ data—we observed WGD in an average of 13% of all sequenced cells from cell lines, 4.7% of all cells from sequenced PDXs and 18% of all cells from

sequenced primary tumors (Extended Data Fig. 3a). Interestingly, there was only a small difference in the number of mtDNA variants in diploid and tetraploid cells (Supplementary Table 4). On the other hand, tetraploid cells had significantly higher mtDNA copy numbers than diploid cells across all cell lines, PDX models and primary tumor

samples (two-sample Wilcoxon test, all $P < 10^{-15}$; Fig. 3a and Extended Data Fig. 3b).

Because coordinated transcription between the nuclear and mitochondrial genomes is necessary for proper stoichiometric assembly of respiratory complexes^{36–38}, we tested whether the mtDNA copy number would increase in direct proportion to the ploidy of the nuclear genome³⁹ (Methods). To do so, we investigated how MNR varies in tetraploid versus diploid populations of related subclones in a common sequencing library. In parental 184-hTERT cells, the MNR difference between diploid and tetraploid cells was negligible ($\log_2(\text{fold change}) = 7.5 \times 10^{-3}, P = 0.067$; Extended Data Fig. 3c). Similar marginal differences in MNR were observed between tetraploid versus diploid cells in most 184-hTERT-derived lines, with the exception of *BRCA1*-null 184-hTERT cells that exhibited 31% (SA1292) and 15% (SA1054) increases in MNR in tetraploid cells relative to diploid cells (one-sided Wilcoxon test, $P = 9.3 \times 10^{-4}$ and $P = 2.4 \times 10^{-7}$, respectively; Fig. 3b). We observed a similar tendency for preservation or small increases in MNR in tetraploid cells relative to diploid cells in the majority of eight PDX and primary tumor samples with sufficient tetraploid/diploid cells for analysis (percent change –6.3% to 12.6%; 2/8 samples statistically significant: one-sided Wilcoxon test, both $P < 0.025$; Fig. 3c). These data establish that for the majority of samples, tetraploid cells and diploid cells derived from a common progenitor contain roughly equal numbers of mtDNA copies per haploid genome. This dosage homeostasis between mtDNA and nuDNA is remarkable especially because mtDNA replication has generally been thought to be uncoupled from the nuDNA replication^{40,41}, however, recent studies suggest additional preferential mtDNA replication during S phase^{42,43}. Through fluorescence-activated cell sorting (FACS)-based isolation of cells from T-47D breast cancer and GM18507 lymphoblastoid cell lines, we investigated the relationship between absolute mtDNA copy number and nuDNA ploidy across cell cycle phases and found that the mtDNA copy number was preferentially replicated in the S phase. This resulted in a higher mtDNA copy number, but not MNR, in the G2 and S phases compared to the G1 phase (Extended Data Fig. 3d,e). Additionally, while the mtDNA copy number was approximately doubled in the presence of a WGD, the increase in cell diameter was not as pronounced, indicating that MNR homeostasis is not completely explained by adaptations in cell size (Extended Data Fig. 3f,g). Together, these results suggest that a combination of passive and active mechanisms homeostatically coordinate absolute mtDNA copy number and nuDNA ploidy. We subsequently focused on investigating the factors driving exceptions to this phenomenon.

To better understand why some samples exhibited large increases in MNR in tetraploid cells relative to diploid cells, we investigated in detail the *TP53*^{−/−} 184-hTERT sample SA906a and the primary HGSC tumor SPECTRUM-OV-081, both of which demonstrated large, statistically significant differences in tetraploid versus diploid MNR (9.35% and 12.6%, respectively; one-sided Wilcoxon test, both $P < 1.2 \times 10^{-4}$). We hypothesized that, in these samples, high levels of clonal diversification produced clones with distinct MNR that could indirectly produce an apparent difference between MNR in diploid and tetraploid cells. To test this hypothesis, we ran HDBSCAN⁴⁴ to detect clusters of cells with similar nuDNA copy number profiles and assigned each cell to a specific clone. Somatic mtDNA variants determined to be informative based on a Bayesian clonal assignment model were present in both diploid and tetraploid cells of the same clones, confirming the presence of both diploid and tetraploid cells within a clone (Methods; Extended Data Fig. 3h–k). Consistent with our hypothesis, we observed substantial differences in the MNR of clone A in SA906a, which is primarily distinguished by the presence of a *MYC* focal amplification, compared to ancestral clone D ($\log_2(\text{fold change}) = 0.5$, Wilcoxon test, $P < 2.2 \times 10^{-16}$). Notably, diploid and tetraploid cells in the same clone demonstrated indistinguishable MNRs, whereas the differences in MNR between ploidy-matched diploid cells across clones A and D were large and statistically significant ($\log_2(\text{MNR})$ of 0.5, $P < 10^{-15}$; Fig. 3d,e). A similar

effect was observed in the primary tumor sample SPECTRUM-OV-081, where the clonal differences in MNR (for example, in exceptionally high MNR in clone C) dominated intraclone differences in diploid and tetraploid cells (Fig. 3f,g). These data indicate that clonal diversification can drive apparent differences in MNR between diploid and tetraploid cells, and when clonal identity is controlled, diploid and tetraploid cells demonstrate equivalent MNR levels.

High MNR increases interferon (IFN) response and depletes hypoxic gene expression

We next asked if clone-specific differences in MNR elicited phenotypic consequences. We computationally assigned cells in scRNA-seq to clones identified from matched DLP+ using TreeAlign⁴⁵ across samples with both DLP+ and matching scRNA-seq data (Methods). We then compared mtDNA-encoded gene expression patterns of clones with the highest MNR to those with the lowest MNR. For instance, HGSC primary tumor SPECTRUM-OV-022 contained eight clones that closely clustered clones (A, C, D, E, G, I, J and K; Fig. 4a,b). Clone A, which had a high MNR, had higher expression of mtDNA-encoded *MT-CO2* compared to clone I, which had the lowest MNR (Fig. 4c). A similar pattern was observed in SPECTRUM-OV-081, which showed three clones in the UMAP—clones A, B and C (Fig. 4d,e). Clone C (highest MNR) had higher *MT-ND3* expression compared to clone B (lowest MNR; Fig. 4f). We then expanded this analysis across all tumors, comparing tumor subclones for cases with large clonal differences in MNR ($\log_2(\text{MNR}) > 0.15$). For each of the three tumor samples with sufficiently large differences in MNR across clones, we compared the transcriptional profiles of cells in clones with the maximal and minimal MNR (including one PDX and two primary HGSC tumors), observing that transcription of mtDNA-encoded genes was significantly higher in MNR-high clones compared to MNR-low clones (Extended Data Fig. 4a). Similarly, we observed enrichment in mtDNA-encoded gene expression for MNR-high clones for cell lines (Extended Data Fig. 4b). While an association between MNR and mtDNA expression has been suggested in earlier work^{30,46}, these data directly connects subclonal variation in MNR to mtDNA-encoded gene expression.

To more granularly understand the association between MNR and non-mtDNA-encoded gene expression, we undertook a pathway enrichment analysis. Pathway analysis on the three tumor samples with matched DLP+ and scRNA-seq using differential expression between high and low MNR clones identified 8/51 Molecular Signatures Database (MSigDB) hallmark gene sets with recurrent enrichment/depletion, including elevated expression of mtDNA oxidative phosphorylation (OXPHOS) pathway and innate immune-related pathways (Fig. 4g). Interestingly, only SPECTRUM-OV-022 exhibited statistically significant enrichment in nuDNA-encoded OXPHOS in the same direction as mtDNA-encoded OXPHOS, ruling out MNR as a dominant regulator of nuDNA-encoded OXPHOS transcription. Instead, high MNR clones exhibited a recurrent depletion in hypoxic gene expression—in both SPECTRUM-OV-022 and SPECTRUM-OV-081, high MNR clones (OV-022 clone A; OV-081 clone C) had significantly lower PROGENY hypoxia enrichment score than low MNR clones (SPECTRUM-OV-022 clone I; SPECTRUM-OV-081 clone B; Wilcoxon test; OV-022, $P = 0.0064$, OV-081, $P = 7.9 \times 10^{-6}$; Fig. 4h,i). Variation in MNR *in vivo* is thus primarily associated with changes to mtDNA-encoded, but not nuclear-DNA-encoded, OXPHOS expression, as well as transcriptional adaptations to nuDNA-encoded metabolic pathways.

Dosage-dependent mtDNA variant effects on mtDNA copy number

Recently, a genome-wide association study (GWAS) of variation in mtDNA copy number in whole blood reported that certain germline mtDNA insertions, including those affecting the length of a homopolymeric block at m.302 associated with the balance of mtDNA replication and transcription, could potentially regulate mtDNA copy number^{47–49}. Interestingly, this study revealed (using scATAC-seq) that individual

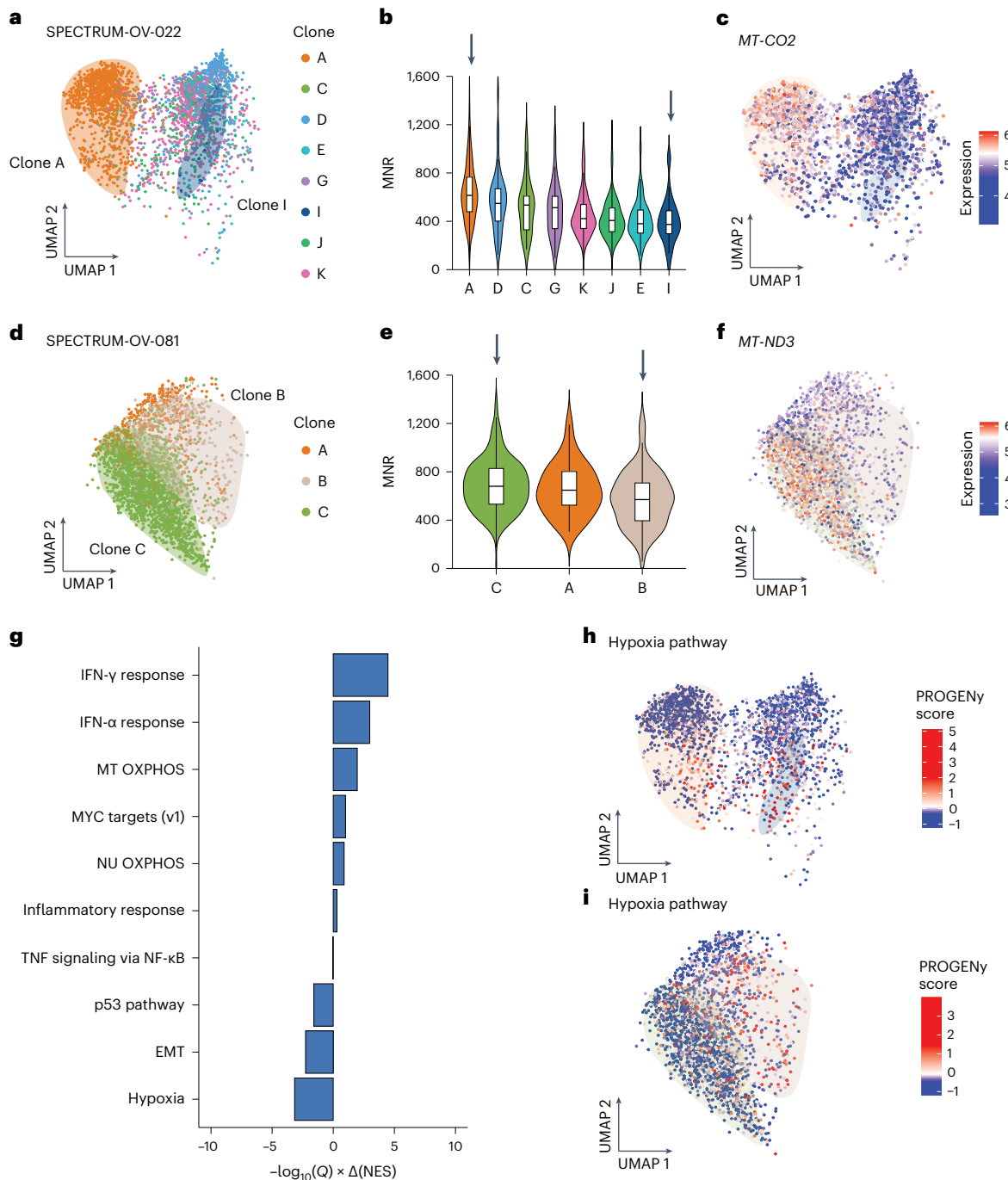


Fig. 4 | Mapping clones between DLP+ and scRNA-seq reveals that high MNR leads to enrichment in IFN signaling and depletion in the hypoxia pathway. **a**, UMAP of scRNA-seq data from SPECTRUM-OV-022, colored by clones inferred from TreeAlign, $n = 2,954$ cells. Shaded areas demarcate clones A and I, with each encompassing cells of the same clone. **b**, Violin plot of per-cell MNR distribution across eight clones ($n = 958$ cells). Arrows refer to clones A and I having the highest and the lowest median MNR values. All boxplots represent the median, 25th percentile and 75th percentile, and whiskers correspond to 1.5 times the interquartile range. **c**, UMAP plot, colored by expression level of MT-CO2, which indicates clone A having the highest expression. Shaded areas demarcate clones A and I, with each encompassing cells from the same clone. **d**, Same as **a** but for SPECTRUM-OV-081, $n = 2,666$ cells. Shaded areas demarcate clones B and C, with each encompassing cells of the same clone. **e**, Violin plot of per-cell MNR distribution across three clones ($n = 700$ cells). Arrows refer to clones C and B having the highest and the lowest median MNR values. All boxplots represent

the median, 25th percentile and 75th percentile, and whiskers correspond to 1.5 times the interquartile range. **f**, UMAP plot, colored by expression level of MT-ND3, which indicates clone C having the highest expression. Shaded areas demarcate clones B and C, with each encompassing cells from the same clone. **g**, Differential expression of MSigDB hallmark gene sets for tumor samples, between clones with the highest and the lowest MNR. Differential expression is quantified by directional $-\log_{10}(Q)$: here >0 denotes upregulation in clones with high MNR; <0 denotes downregulation. EMT, epithelial-mesenchymal transition. **h**, UMAP plot colored by PROGENY score for hypoxia pathway, which indicates a depletion in clone A. Shaded areas demarcate the two clones—A and I, with each encompassing cells from the same clone. **i**, UMAP plot colored by PROGENY score for hypoxia pathway, which indicates a depletion in clone C. Shaded areas demarcate the two clones—B and C, with each encompassing cells from the same clone. TNF, tumor necrosis factor; NF-κB, nuclear factor kappa B.

cells from the same patient often exhibited different heteroplasmic levels of such insertions, suggesting that cell-to-cell variation in mtDNA genotype could, in *cis*, drive variation in mtDNA copy number levels. Because of the unique ability of DLP+ to simultaneously track mtDNA copy number and genotype in phenotypically distinct tumor cells, we evaluated if DLP+ could identify the length heteroplasmy at m.302 and, if so, test the hypothesis that the length heteroplasmy is associated with changes in single-cell mtDNA copy number. For each of the 32 samples in our dataset, we genotyped the mtDNA of individual cells (Methods) and identified cells with homopolymeric insertions at m.302. We identified a single sample (SA1047) with a sufficient number of cells for subsequent analysis (at least 20 diploid cells with minimum coverage of 10 reads at position 302; Fig. 5a). Considering diploid cells only to avoid any confounding effects associated with nuDNA, we quantified both mtDNA copy number and the heteroplasmy of the reference allele (m.302A) and evaluated the association between the two. This analysis revealed that, consistent with the bulk GWAS data, cells with the reference allele (m.302A) demonstrated elevated mtDNA copy number (Wilcoxon test, $P = 0.025$; Fig. 5b), and m.302A heteroplasmy was associated with higher mtDNA copy number (Pearson correlation, $R = 0.17$ and $P = 0.018$; Fig. 5c), indicating that mtDNA genotype itself may modulate mtDNA copy number levels.

We next analyzed truncating mutations in mtDNA, which arise in approximately 20% of all cancers and are thought to impair mitochondrial respiration^{2,7,50}. Prior studies have suggested that somatic truncating mtDNA mutations can also elicit increases in mtDNA copy number^{51–53}. However, because prior analyses were undertaken from bulk sequencing data, there remains little understanding of the adaptive response of mtDNA copy number to single-cell variation in heteroplasmy. Analysis of mtDNA copy number and truncating mtDNA mutations in 11,691 total cells across seven distinct cell lines, five PDX samples and five primary tumor samples identified 23 truncating mutation events spanning across 19 distinct genomic positions and 20 silent mutations spanning across 20 distinct genomic positions (truncating variants shown in Fig. 5d). Consistent with prior reports^{7,54}, these mutations predominantly affected complex I subunits at homopolymeric hotspots (for example, m.12417).

Among the 23 truncating variants across both cell lines and tumors, we identified a statistically significant association between the heteroplasmy of m.6708G>A (encoding a complex IV truncating mutation) and mtDNA copy number ($Q = 2.1 \times 10^{-2}$; Fig. 5e). The pathogenicity and clinical significance of this variant have been reported previously in mitochondrial myopathy and rhabdomyolysis⁵⁵, confirming our prediction that somatic truncating mutations in mtDNA can have deleterious effects on the cellular fitness in the form of increased mtDNA copy number. We corroborated the presence of m.6708G>A in

matched scRNA-seq data (Fig. 5f,g) and, consistent with the positive correlation between heteroplasmy and mtDNA copy number observed in DLP+ (Fig. 5h), the heteroplasmy of m.6708G>A in scRNA-seq data was positively associated with the expression of mtDNA-encoded genes (Pearson correlation against mtDNA copy number, $P < 2.2 \times 10^{-16}$; against *MT-ND3* expression, $P < 0.001$; Fig. 5i–k). In contrast, we found no statistically significant association between heteroplasmy and mtDNA copy number levels among 20 silent mutations. Finally, we also evaluated the association between the heteroplasmy of 130 nontruncating mitochondrial variants, the vast majority of which were variants of unknown significance, and mtDNA copy number. This identified two variants (m.822G>A, affecting a nearly universally conserved locus of *MT-RNR1*, and m.10197G>A, a confirmed-pathogenic allele causing Leigh disease^{56,57}) whose heteroplasmy significantly associated with elevated mtDNA copy number, implicating these mutations as putative modifiers of resting mtDNA copy number. A fourth variant of unknown significance (m.1150G>A, also affecting *MT-RNR1* and universally conserved in the human germline) was observed in two *TP53*^{-/-} 184-hTERT cell lines and associated with decreased mtDNA copy number. These data establish that single cells adapt to some pathogenic mtDNA mutations, but not silent mutations, by increasing mtDNA copy number in a heteroplasmy/dosage-dependent manner.

Discussion

Although the few proteins encoded by mtDNA are essential to normal cellular metabolism and physiology, both mtDNA copy number and genotype can vary dramatically across otherwise isogenic populations of cells. Neither the regulatory principles controlling this cell-to-cell variation nor the phenotypes arising from variation in mtDNA copy number in individual cells are well-understood. By applying DLP+ to simultaneously characterize mtDNA copy number, mtDNA genotype and nuDNA genotype in >72,000 cells, we were able to carry out scaled analyses of the biophysical, evolutionary and phenotypic consequences of cell-to-cell variation in mtDNA copy number.

We observed extensive variation in per-cell mtDNA copy number, which is consistent with previous observations^{24,25}. By characterizing the quantitative variation in per-cell mtDNA copy number in human cancer in relation to cell size, nuclear ploidy, clonal composition and expression of mtDNA-encoded OXPHOS genes, we have shown that mtDNA copy number variation reflects, at least in part, both anabolic cellular demands for increased levels of cellular building blocks to produce larger cells⁵⁸ and stoichiometric equipoise to ensure appropriate relative levels of mtDNA and nuDNA³⁶ (that is, the MNR). Remarkably, the emergence of genetically distinct subclones can perturb MNR levels, and such variation in MNR appears to have specific transcriptional consequences on mtDNA-derived, but not

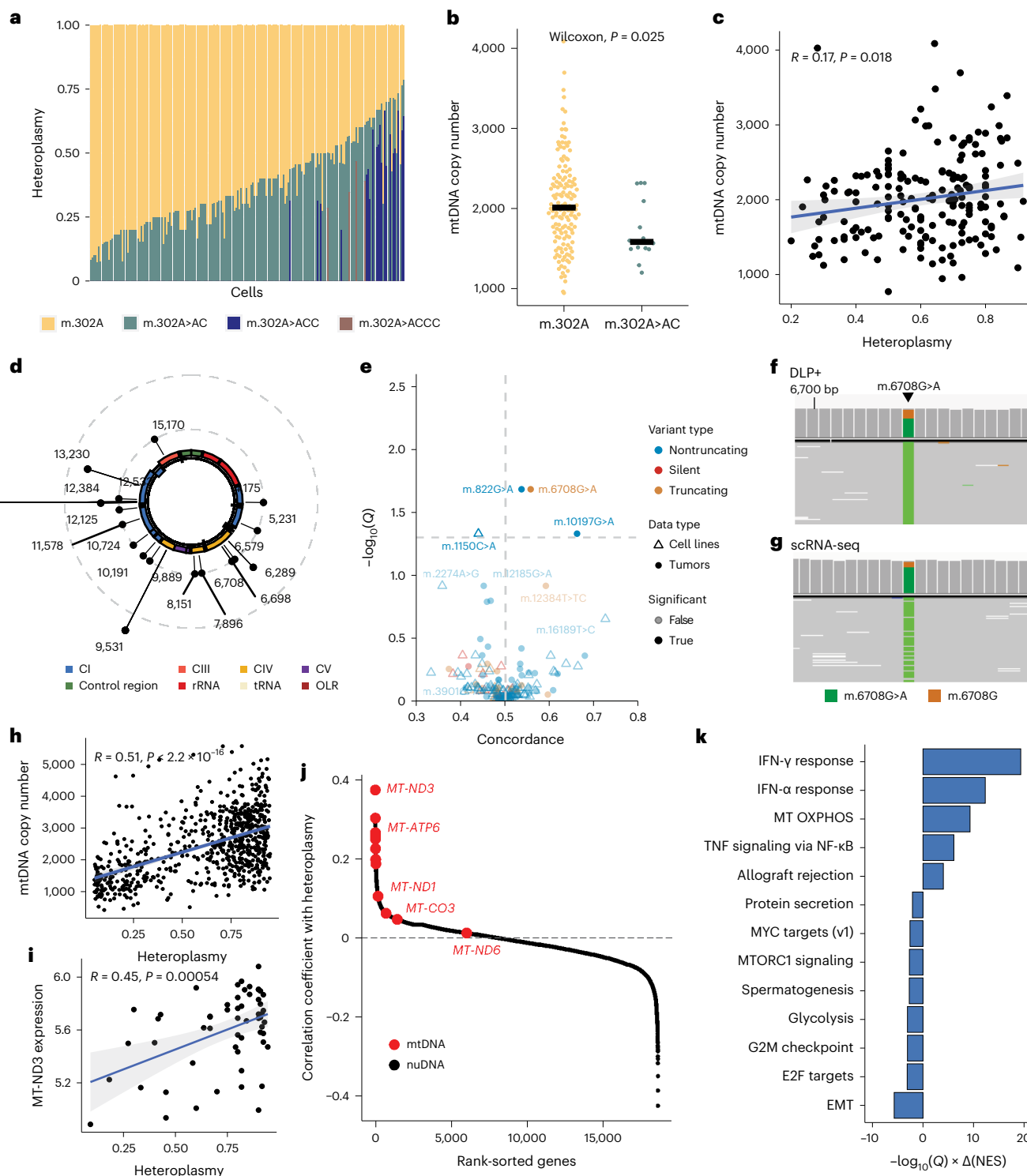
Fig. 5 | Genetic perturbation in mtDNA can elicit a dosage-dependent decrease in mtDNA copy number. **a**, Length heteroplasmy composition of m.302 across 126 single cells in HGSC primary tumor sample, SA1047. Each bar represents a cell. **b**, Effect of length heteroplasmy composition, the reference ($n = 148$ cells) and the major allele ($n = 14$ cells), at m.302 on mtDNA copy number. Reported P value from two-sided, two-sample Wilcoxon signed rank test. **c**, Scatter plot showing heteroplasmy of the reference allele at m.302 and mtDNA copy number (two-sided Pearson correlation, $R = 0.17$, $P < 0.02$). Gray-shaded areas represent error bands indicating the 95% confidence interval, and the blue line indicates the regression line. **d**, Circos plot with lollipop indicating the genomic position of truncating variants identified in DLP+ across both cell lines and PDX models (CI, CIII, CIV, CV, control region, rRNA, tRNA, OLR). **e**, Concordance between the heteroplasmy level of the truncating, silent and nontruncating variants and the mtDNA copy number across all cell lines and tumors. **f**, Integrative Genomics Viewer⁵⁹ of m.6708G>A substitution in DLP+ sequencing data of SPECTRUM-OV-081 Infracolic Omentum sample. The stacked histogram on top reflects the distribution of the reads supporting the reference and the alternate alleles. **g**, Same as f but for scRNA-seq of the same

sample at the matched site. **h**, Two-sided Pearson correlation between mtDNA copy number and heteroplasmy level of the m.6708 truncating variant in SPECTRUM-OV-081 in DLP+ ($R = 0.51$, $P = 2.9 \times 10^{-48}$). Gray-shaded areas represent error bands indicating the 95% confidence interval, and the blue line indicates the regression line. **i**, Two-sided Pearson correlation between *MT-ND3* gene expression and heteroplasmy level of the same m.6708G>A truncating variant in SPECTRUM-OV-081 in matched scRNA-seq ($R = 0.45$, $P = 0.000054$). Gray-shaded areas represent error bands indicating the 95% confidence interval, and the blue line indicates the regression line. **j**, Pearson correlation coefficient between the heteroplasmy level of the truncating variant m.6708 and expression of all the genes in the SPECTRUM-OV-081 sample. The mtDNA-encoded genes are colored in red. **k**, Enrichment of MSigDB hallmarks gene sets for tumors using the rank-sorted gene list based on correlation coefficient, quantified by directional $-\log_{10}(Q)$: here >0 denotes upregulation in cells with high heteroplasmy truncating variants and <0 denotes downregulation. CI, mitochondrial complex I; CIII, mitochondrial complex III; CIV, mitochondrial complex IV; CV, mitochondrial complex V; rRNA: ribosomal RNA; tRNA, transfer RNA; OLR, light strand origin of replication.

nuDNA-derived, OXPHOS transcription. This represents a previously poorly considered class of phenotypic variation that arises from clonal evolution in cancer with potential implications for improved understanding of cellular fitness.

We also find, in agreement with the population-scale analysis of healthy individuals and patients with cancer, that certain mtDNA genotypes were themselves associated with changes to copy number⁴⁷. Unlike bulk sequencing studies, we harnessed DLP+ to quantitatively interrogate how mutant dosage, or mtDNA heteroplasmy, in individual cells affected mtDNA copy number. We observed that both relatively common germline polymorphisms (at m.302) and highly pathogenic

somatic mutations elicited adaptive increases in mtDNA copy number in a heteroplasmy-dependent manner. Given that disruption of different functional components of mtDNA (such as complex I versus complex IV subunits or tRNA genes versus protein-coding genes) is known to produce vastly different phenotypes and sensitively depend on cell-of-origin, investigation of the adaptive mtDNA copy number response to functionally distinct mtDNA mutations in diverse cellular backgrounds may prove insightful. In summary, our work here implicates the coevolution of the mitochondrial and nuclear genomes in individual cells as a regulator of cellular fitness and phenotypic states in cancer.



Online content

Any methods, additional references, Nature Portfolio reporting summaries, source data, extended data, supplementary information, acknowledgements, peer review information; details of author contributions and competing interests; and statements of data and code availability are available at <https://doi.org/10.1038/s41588-024-01724-8>.

References

1. Reznik, E. et al. Mitochondrial DNA copy number variation across human cancers. *eLife* **5**, e10769 (2016).
2. Yuan, Y. et al. Comprehensive molecular characterization of mitochondrial genomes in human cancers. *Nat. Genet.* **52**, 342–352 (2020).
3. Gaude, E. et al. NADH shuttling couples cytosolic reductive carboxylation of glutamine with glycolysis in cells with mitochondrial dysfunction. *Mol. Cell* **69**, 581–593 (2018).
4. Vyas, S., Zaganjor, E. & Haigis, M. C. Mitochondria and cancer. *Cell* **166**, 555–566 (2016).
5. Shidara, Y. et al. Positive contribution of pathogenic mutations in the mitochondrial genome to the promotion of cancer by prevention from apoptosis. *Cancer Res.* **65**, 1655–1663 (2005).
6. Park, J. S. et al. A heteroplasmic, not homoplasmic, mitochondrial DNA mutation promotes tumorigenesis via alteration in reactive oxygen species generation and apoptosis. *Hum. Mol. Genet.* **18**, 1578–1589 (2009).
7. Gorelick, A. N. et al. Respiratory complex and tissue lineage drive recurrent mutations in tumour mtDNA. *Nat. Metab.* **3**, 558–570 (2021).
8. Filograna, R. et al. Modulation of mtDNA copy number ameliorates the pathological consequences of a heteroplasmic mtDNA mutation in the mouse. *Sci. Adv.* **5**, eaav9824 (2019).
9. Stewart, J. B. & Chinnery, P. F. The dynamics of mitochondrial DNA heteroplasmy: implications for human health and disease. *Nat. Rev. Genet.* **16**, 530–542 (2015).
10. Wei, W. et al. Germline selection shapes human mitochondrial DNA diversity. *Science* **364**, eaau6520 (2019).
11. Chinnery, P. F., Samuels, D. C., Elson, J. & Turnbull, D. M. Accumulation of mitochondrial DNA mutations in ageing, cancer, and mitochondrial disease: is there a common mechanism? *Lancet* **360**, 1323–1325 (2002).
12. Kang, E. et al. Age-related accumulation of somatic mitochondrial DNA mutations in adult-derived human iPSCs. *Cell Stem Cell* **18**, 625–636 (2016).
13. Ludwig, L. S. et al. Lineage tracing in humans enabled by mitochondrial mutations and single-cell genomics. *Cell* **176**, 1325–1339 (2019).
14. Lareau, C. A. et al. Massively parallel single-cell mitochondrial DNA genotyping and chromatin profiling. *Nat. Biotechnol.* **39**, 451–461 (2020).
15. Miller, T. E. et al. Mitochondrial variant enrichment from high-throughput single-cell RNA-seq resolves clonal populations. *Nat. Biotechnol.* **40**, 1030–1034 (2021).
16. Xu, J. et al. Single-cell lineage tracing by endogenous mutations enriched in transposase accessible mitochondrial DNA. *eLife* **8**, e45105 (2019).
17. Jiang, M. et al. Increased total mtDNA copy number cures male infertility despite unaltered mtDNA mutation load. *Cell Metab.* **26**, 429–436 (2017).
18. Grady, J. P. et al. mtDNA heteroplasmy level and copy number indicate disease burden in m.3243A>G mitochondrial disease. *EMBO Mol. Med.* **10**, e8262 (2018).
19. Salehi, S. et al. Clonal fitness inferred from time-series modelling of single-cell cancer genomes. *Nature* **595**, 585–590 (2021).
20. Funnell, T. et al. Single-cell genomic variation induced by mutational processes in cancer. *Nature* **612**, 106–115 (2022).
21. Laks, E. et al. Clonal decomposition and DNA replication states defined by scaled single-cell genome sequencing. *Cell* **179**, 1207–1221 (2019).
22. Ju, Y. S. et al. Origins and functional consequences of somatic mitochondrial DNA mutations in human cancer. *eLife* **3**, e02935 (2014).
23. Burr, S. P. & Chinnery, P. F. Measuring single-cell mitochondrial DNA copy number and heteroplasmy using digital droplet polymerase chain reaction. *J. Vis. Exp.*, <https://doi.org/10.3791/63870> (2022).
24. Müller-Höcker, J. et al. Oxyphil cell metaplasia in the parathyroids is characterized by somatic mitochondrial DNA mutations in NADH dehydrogenase genes and cytochrome c oxidase activity-impaired genes. *Am. J. Pathol.* **184**, 2922–2935 (2014).
25. Cree, L. M. et al. A reduction of mitochondrial DNA molecules during embryogenesis explains the rapid segregation of genotypes. *Nat. Genet.* **40**, 249–254 (2008).
26. Reber, S. & Goehring, N. W. Intracellular scaling mechanisms. *Cold Spring Harb. Perspect. Biol.* **7**, a019067 (2015).
27. Rafelski, S. M. et al. Mitochondrial network size scaling in budding yeast. *Science* **338**, 822–824 (2012).
28. Miettinen, T. P. & Björklund, M. Cellular allometry of mitochondrial functionality establishes the optimal cell size. *Dev. Cell* **39**, 370–382 (2016).
29. Miettinen, T. P. & Björklund, M. Mitochondrial function and cell size: an allometric relationship. *Trends Cell Biol.* **27**, 393–402 (2017).
30. D’Erchia, A. M. et al. Tissue-specific mtDNA abundance from exome data and its correlation with mitochondrial transcription, mass and respiratory activity. *Mitochondrion* **20**, 13–21 (2015).
31. Basu, A., Lenka, N., Mullick, J. & Avadhani, N. G. Regulation of murine cytochrome oxidase Vb gene expression in different tissues and during myogenesis. Role of a YY-1 factor-binding negative enhancer. *J. Biol. Chem.* **272**, 5899–5908 (1997).
32. Seel, A. et al. Regulation with cell size ensures mitochondrial DNA homeostasis during cell growth. *Nat. Struct. Mol. Biol.* **30**, 1549–1560 (2023).
33. Osman, C., Noriega, T. R., Okreglak, V., Fung, J. C. & Walter, P. Integrity of the yeast mitochondrial genome, but not its distribution and inheritance, relies on mitochondrial fission and fusion. *Proc. Natl Acad. Sci. USA* **112**, E947–E956 (2015).
34. Galitski, T., Salданha, A. J., Styles, C. A., Lander, E. S. & Fink, G. R. Ploidy regulation of gene expression. *Science* **285**, 251–254 (1999).
35. Comai, L. The advantages and disadvantages of being polyploid. *Nat. Rev. Genet.* **6**, 836–846 (2005).
36. Soto, I. et al. Balanced mitochondrial and cytosolic translomes underlie the biogenesis of human respiratory complexes. *Genome Biol.* **23**, 170 (2022).
37. Couvillion, M. T., Soto, I. C., Shipkovenska, G. & Churchman, L. S. Synchronized mitochondrial and cytosolic translation programs. *Nature* **533**, 499–503 (2016).
38. Lazarou, M., McKenzie, M., Ohtake, A., Thorburn, D. R. & Ryan, M. T. Analysis of the assembly profiles for mitochondrial- and nuclear-DNA-encoded subunits into complex I. *Mol. Cell. Biol.* **27**, 4228–4237 (2007).
39. Gyorffy, M. F. et al. Nuclear–cytoplasmic balance: whole genome duplications induce elevated organellar genome copy number. *Plant J.* **108**, 219–230 (2021).
40. Pica-Mattoccia, L. & Attardi, G. Expression of the mitochondrial genome in HeLa cells. IX. Replication of mitochondrial DNA in relationship to cell cycle in HeLa cells. *J. Mol. Biol.* **64**, 465–484 (1972).
41. Antes, A. et al. Differential regulation of full-length genome and a single-stranded 7S DNA along the cell cycle in human mitochondria. *Nucleic Acids Res.* **38**, 6466–6476 (2010).

42. Chatre, L. & Ricchetti, M. Prevalent coordination of mitochondrial DNA transcription and initiation of replication with the cell cycle. *Nucleic Acids Res.* **41**, 3068–3078 (2013).
43. Sasaki, T., Sato, Y., Higashiyama, T. & Sasaki, N. Live imaging reveals the dynamics and regulation of mitochondrial nucleoids during the cell cycle in Fucci2-HeLa cells. *Sci. Rep.* **7**, 11257 (2017).
44. McInnes, L., Healy, J. & Astels, S. Hdbscan: hierarchical density based clustering. *J. Open Source Softw.* **2**, 205 (2017).
45. Campbell, K. R. et al. clonealign: statistical integration of independent single-cell RNA and DNA sequencing data from human cancers. *Genome Biol.* **20**, 54 (2019).
46. Yang, S. Y. et al. Blood-derived mitochondrial DNA copy number is associated with gene expression across multiple tissues and is predictive for incident neurodegenerative disease. *Genome Res.* **31**, 349–358 (2021).
47. Gupta, R. et al. Nuclear genetic control of mtDNA copy number and heteroplasmy in humans. *Nature* **620**, 839–848 (2023).
48. Nekhaeva, E. et al. Clonally expanded mtDNA point mutations are abundant in individual cells of human tissues. *Proc. Natl Acad. Sci. USA* **99**, 5521–5526 (2002).
49. Herbst, A. et al. Accumulation of mitochondrial DNA deletion mutations in aged muscle fibers: evidence for a causal role in muscle fiber loss. *J. Gerontol. A Biol. Sci. Med. Sci.* **62**, 235–245 (2007).
50. Mahmood, M. et al. Mitochondrial DNA mutations drive aerobic glycolysis to enhance checkpoint blockade response in melanoma. *Nat. Cancer.* <https://doi.org/10.1038/s43018-023-00721-w> (2024).
51. De Grey, A. D. A proposed refinement of the mitochondrial free radical theory of aging. *Bioessays* **19**, 161–166 (1997).
52. Shigenaga, M. K., Hagen, T. M. & Ames, B. N. Oxidative damage and mitochondrial decay in aging. *Proc. Natl Acad. Sci. USA* **91**, 10771–10778 (1994).
53. DeHaan, C. et al. Mutation in mitochondrial complex I ND6 subunit is associated with defective response to hypoxia in human glioma cells. *Mol. Cancer* **3**, 19 (2004).
54. Kollberg, G., Moslemi, A.-R., Lindberg, C., Holme, E. & Oldfors, A. Mitochondrial myopathy and rhabdomyolysis associated with a novel nonsense mutation in the gene encoding cytochrome c oxidase subunit I. *J. Neuropathol. Exp. Neurol.* **64**, 123–128 (2005).
55. Sazanov, L. *A Structural Perspective on Respiratory Complex I: Structure and Function of NADH:Ubiquinone Oxidoreductase* (Springer Science & Business Media, 2012).
56. Chae, J. H. et al. A novel ND3 mitochondrial DNA mutation in three Korean children with basal ganglia lesions and complex I deficiency. *Pediatr. Res.* **61**, 622–624 (2007).
57. O’Hara, R. et al. Quantitative mitochondrial DNA copy number determination using droplet digital PCR with single-cell resolution. *Genome Res.* **29**, 1878–1888 (2019).
58. Schmoller, K. M. & Skotheim, J. M. The biosynthetic basis of cell size control. *Trends Cell Biol.* **25**, 793–802 (2015).
59. Robinson, J. T. et al. Integrative genomics viewer. *Nat. Biotechnol.* **29**, 24–26 (2011).

Publisher’s note Springer Nature remains neutral with regard to jurisdictional claims in published maps and institutional affiliations.

Open Access This article is licensed under a Creative Commons Attribution 4.0 International License, which permits use, sharing, adaptation, distribution and reproduction in any medium or format, as long as you give appropriate credit to the original author(s) and the source, provide a link to the Creative Commons licence, and indicate if changes were made. The images or other third party material in this article are included in the article’s Creative Commons licence, unless indicated otherwise in a credit line to the material. If material is not included in the article’s Creative Commons licence and your intended use is not permitted by statutory regulation or exceeds the permitted use, you will need to obtain permission directly from the copyright holder. To view a copy of this licence, visit <http://creativecommons.org/licenses/by/4.0/>.

© The Author(s) 2024

Methods

Experimental model and participant details

Cell culture and PDXs. Cell lines were generated as previously described^{19,21}. In brief, the samples included (1) an immortalized normal human female breast epithelial cell line 184-hTERT L9, (2) four sets of 184-hTERT cell lines with perturbations in *TP53*^{+/−} passaged over multiple time points, (3) five 184-hTERT cell lines with a variety of genetic perturbations in the repair pathway, including *TP53*^{+/−}, *BRCA1*^{+/−}, *BRCA2*^{+/−} and *BRCA2*^{+/−} and (4) a GM18507 lymphoblastoid cell line. The samples also included three sets of TNBC PDX models. The University of British Columbia's Ethics Committees granted approval for all experiments involving human resources. Donors from Vancouver, British Columbia, provided their consent for the Tumor Tissue Repository protocols (TTR-H06-00289, H16-01625). These samples were then transplanted into mice following the Animal Resource Center bioethics protocol (A19-0298-A001), which received approval from both the University of British Columbia's Animal Care Committee and the BC Cancer Research Ethics Board under protocols H20-00170 and H18-01113. The serial passaging was done by seeding approximately 1 million cells each time and profiled with DLP+ at 4–11 different passage points with a mean of 6,070 cells at each time point.

SPECTRUM. All patients from the MSK SPECTRUM cohort^{60–62} provided their consent to the institutional biospecimen banking protocol. The Memorial Sloan Kettering Cancer Center's Institutional Review Board (IRB) approved all related protocols (15-200 and 06-107). The consent process adhered to the IRB's standard operating procedures for obtaining informed consent, ensuring that all participants were fully informed and agreed in writing before any study-specific activities commenced. This study was carried out in accordance with the principles of the Declaration of Helsinki and adhered to the Good Clinical Practice guidelines. Matched 10x Genomics 3'-end scRNA-seq and DLP+ were obtained from two patients with HGSC (OV-022 and OV-081). Single-cell suspensions were flow-sorted on CD45 to separate the immune component, and the CD45-negative fractions were then profiled with DLP+.

Quantification and statistical analysis

Mitochondrial variant calling and genotyping. Quality score is assigned to each cell as part of the DLP+ pipeline based on 18 features related to read depth and nuDNA CNV information, as described in ref. 21. Only live cells with a quality score of at least 0.75 were kept for further analysis. We developed a single-cell variant calling workflow to identify mtDNA variants in single cells based on our previously described variant calling pipeline⁷. Variants are called by two independent variant-calling pipelines, and only the variants identified by both pipelines were retained for further analysis. The first pipeline is Mutect2 (GATK v4.1.2.0) using the mitochondrial option, which was run on every cell and then merged into a single VCF file. The second pipeline is samtools mpileup (v1.9) to generate a pileup file using variant-supporting reads with a minimum mapping quality (>20) and base quality (>20). This was run on the merged pseudo-bulk of all the single cells for the variant calling step. Variants were required to contain at least two variant-supporting reads in both the forward and reverse directions. PCR duplicates and reads that failed any of the quality checks were removed. As described in ref. 14, capturing the agreement of heteroplasmy between the strands is important in eliminating false positive calls. Thus, variants were further filtered based on a high Pearson correlation ($R \geq 0.2$). Next, the black-listed, homopolymer repeat regions (513–525 and 3105–3109) in the mtDNA genome were filtered out as well²². The filtered variants were genotyped by running the second pipeline on individual cells for a per-cell heteroplasmy calculation. Mutational signature and strand bias were assessed as described in ref. 22,63. The trinucleotide sequence context (immediate 5' and 3') was extracted, and the substitution rate for each context was calculated with the number of substitutions normalized by the frequency of all the observed contexts, in the L and H strand,

respectively. We defined the germline variants as variants that enable us to infer the ancestral haplogroup for each cell line. Homoplasmic variants then refer to variants that are not found in the haplogroup of the sample (local private mutations) or in any of the defined haplogroups (global private mutations).

Estimation of average nuclear ploidy and baseline ploidy. Both the average ploidy and the baseline ploidy level of each cell were estimated with HMMcopy⁶⁴, as previously described in ref. 21. Briefly, for each cell, we calculate the average ploidy as the mean copy number across the 500 kilobase-wide bins in the entire nuclear genome, which is a nonnegative real number. On the other hand, the baseline ploidy of cells is categorized as either diploid, triploid, tetraploid or some other integer value based on the most commonly occurring copy number state across the 500 kilobase-wide bins of the entire nuclear genome.

Estimation of mtDNA gross copy number. The mtDNA copy number was calculated for each cell as follows:

$$\text{mtDNA copy number} = \frac{\text{mtDNA read depth}}{\text{nuDNA read depth}} \times \text{average ploidy}$$

The MNR refers to the ratio of mtDNA read depth to nuDNA read depth. Average ploidy was calculated using the mean copy number of all bins across the nuDNA genome from the HMMcopy⁶⁴ result.

Determining the cell diameter from microscopic images. DLP+ platform has microscopic image data at the nozzle before the cells are isolated into wells²¹. Microscopic images taken during the dispensing of the cells are used to automatically filter for doublets, and additional manual inspection of tetraploid cell images found that the median number of doublets across 25 sequencing libraries was 3.76%, suggesting that WGD predictions are unlikely to be confounded by doublets (Extended Data Fig. 2h,i and Supplementary Table 3). The diameter was calculated as Waddel disk diameter²¹.

A linear regression model for inference of cell size. First, a linear regression model was built to predict mtDNA copy number from the average nuDNA ploidy. Then the model was expanded to a linear multiple regression model to predict mtDNA copy number from cell diameter and the average ploidy. The average ploidy level could deviate from the integer baseline ploidy level in the presence of large chromosomal arm level copy number changes. Benjamini–Hochberg correction was applied for each sequencing library to account for the multiple testing of cells. For plotting, the scale was standardized and normalized to the mean.

Comparison of mtDNA copy number across cell cycle phases. Cell cycle analysis was performed on T-47D and GM18507 cell lines generated through the combination of experimental FACS²¹ and PERT⁶² output. FACS cell cycle phase labels were derived by staining cells for their total DNA content using DAPI and then isolating cells into G1-, S- and G2-phase populations before sequencing. PERT was then run on this scWGS data at 500 kb resolution using default model parameters and the FACS labels as initializations for the G1/2- and S-phase populations. PERT calls cells with 5–95% replicated loci as S phase and all others as G1/2 phase. The fraction of replicated loci per cell is also used to scale the total copy number of these cells. Only cells with matching FACS and PERT phase labels were included in the downstream analysis.

Relative change in MNR between diploid and tetraploid cells. The change in the MNR was calculated for each group as follows:

$$\text{Difference} = \frac{\text{Median}(\text{MNR}_t) - \text{Median}(\text{MNR}_d)}{\text{Median}(\text{MNR}_d)} \times 100$$

Inference of clones based on nuDNA read counts. Clonal assignment of the cells was done by running HDBSCAN on the two-dimensional embedding from UMAP of the per-cell GC-corrected read count profiles²⁰. Parameters used in UMAP and HDBSCAN were the same as previously described—UMAP was run with `min_dist = 0.0` and `metric = 'correlation'`, whereas HDBSCAN was run with `approx_min_span_tree = False`, `cluster_selection_epsilon = 0.2` and `gen_min_span_tree = True`.

Model description and clonal inference using mtDNA variants. MityBayes is a Bayesian statistical model that systematically assigns cells into clones based on both the presence of mtDNA mutations and their heteroplasmy levels. The inputs to MityBayes are a prior on the number of clones, alternate read counts and the total read counts for each mtDNA variant across the cells. The alternate read counts of a variant in a cell follow a binomial distribution. The total read count at a specific genomic position where a variant is present is equivalent to the number of trials (n) and the clone-specific heteroplasmy level serves as the probability of success (p). Inference is performed using stochastic variational inference in the Pyro package. We generate the variational distributions using the AutoDelta function that uses Delta distributions to construct a MAP guide over the latent space. Optimization is performed using the Adam optimizer. By default, we set a learning rate of 0.1, and the convergence is determined when the relative change in evidence lower bound (ELBO) is lower than 10^{-5} . We benchmarked MityBayes against the most similar method available in the literature, MQuad⁶⁵, which does not assign cells to clones based on mtDNA as MityBayes does but rather prioritizes mtDNA mutations that discriminate among different clones. MityBayes weighed the true variants with a higher probability of contribution in the clone assignment and was able to detect the clones when the input variants list was filtered (Extended Data Fig. 3l,m).

Integration of scDNA and scRNA data with TreeAlign. TreeAlign was used to computationally integrate scDNA and scRNA data by assigning transcriptional profiles to scDNA-based subclones. Briefly, TreeAlign explicitly models clone-specific copy number dosage effects and defines subclones informed by transcriptional changes from scDNA-based single-cell phylogenies. Here we ran TreeAlign with the following parameters: `infer_b_allele = False`, `repeat = 8`, `min_clone_assign_prob = 0.9`, `min_clone_assign_freq = 0.75`, `min_consensus_gene_freq = 0.55`, `max_iter = 900`, `rel_tol = 1e-5`, `initialize_seed = True`, `min_cell_count_expr = 40`, `min_cell_count_cnv = 30`, `min_gene_diff = 150`, `min_snp_diff = 60`, `level_cutoff = 50`, `min_proceed_freq = 0.80`, `min_record_freq = 0.75`.

Pathway enrichment analysis in matched scRNA-seq. CellRanger software (version 4.0.0) was used to perform read alignment, barcode filtering and UMI quantification using the 10 \times GRCh38 transcriptome (version 3.0.0) for gene expression. Filtered matrices were processed using the Seurat R package (version 3.0.1)^{66,67}. The resulting gene-by-cell matrix was log normalized and merged by the patient. Cell-type assignments were computed on each patient with cellsign (version 0.99.2)⁶⁸ using a set of curated marker genes, and cancer cells with a high probability (>0.99) were retained. Clone labels were assigned from using CNV data obtained from DLP+ using CloneAlign (version 0.99.0)⁴⁵. Cell-type annotated matrices for individual patients across time points were integrated with Harmony (version 0.1)⁶⁹ into a single batch-corrected matrix. Dimensionality reduction and visualization as a UMAP embedding were performed with the Seurat R package. Differentially expressed genes ($P < 0.001$, $\log(\text{fold change}) > 0.25$) were computed using the Wilcoxon test using clone labels.

Concordance between mtDNA copy number and heteroplasmy. Because there are multiple sequencing libraries per sample with cells of different average ploidy, we used a stratified and weighted concordance model to identify pairs of heteroplasmy and mtDNA copy

numbers that were consistently associated. Similar to Kendall's Tau, concordance is a nonparametric measure of correlation that relies on the concept of concordant pairs⁷⁰. The concordance analysis was adapted from ref. 71. Briefly, the calculation was done using the concordance function from the survival R package⁷². As with Somers' D and Kendall's tau, the magnitude of c_{scaled} captures the strength of the effect, with values near -1 or 1 corresponding to strong discordance and concordance, respectively. We weighed each observation by the number of cells in the corresponding library. A Z score was computed as unscaled concordance minus 0.5 and divided by the square root of the variance, and the resulting value was used to derive a two-tailed P value. P values were then corrected for multiple testing using the Benjamini–Hochberg method to control the false discovery rate. We filtered for highly covered mtDNA variants with at least ten reads supporting the alternate allele. For each variant, we filtered cells with heteroplasmy less than 0.05 or greater than 0.95 to prevent clusters of cells near 0 or 1 heteroplasmy from erroneously skewing the correlation estimation. Only the variants that had a range of 0.15 were kept for downstream analysis.

Reporting summary

Further information on research design is available in the Nature Portfolio Reporting Summary linked to this article.

Data availability

The sequencing data associated with the study spans already publicly available datasets^{19–21} and are available at the European Genome-Phenome Archive with the accessions EGAS00001006343, EGAS00001004448 and EGAS00001003190. The DLP+ and matching scRNA-seq data for the two patients with HGSC (patient 022 and patient 081) from the MSK SPECTRUM cohort are available via dbGaP (accession phs002857.v2.p1). The processed data are available on Zenodo (<https://doi.org/10.5281/zenodo.10498240>)⁷³.

Code availability

Mutect2 (GATK v4.1.2.0), Samtools (v1.9), CellRanger software (v4.0.0), cellsign (v0.99.2) and CloneAlign (v0.99.0) R packages: R (v4.2.3), Seurat R package (v3.0.1) and Harmony (v0.1) were used in this study. Custom R code to regenerate all figures is available on GitHub (<https://github.com/reznik-lab/mtdna-dlp>)⁷⁴ with the relevant data and instructions to execute the code.

References

60. Vázquez-García, I. et al. Ovarian cancer mutational processes drive site-specific immune evasion. *Nature* **612**, 778–786 (2022).
61. Shi, H. et al. Allele-specific transcriptional effects of subclonal copy number alterations enable genotype-phenotype mapping in cancer cells. *Nat. Commun.* **15**, 2482 (2024).
62. Weiner, A. C. et al. Single-cell DNA replication dynamics in genetically unstable cancers. Preprint at bioRxiv <https://doi.org/10.1101/2023.04.10.536250> (2023).
63. Alexandrov, L. B. et al. Signatures of mutational processes in human cancer. *Nature* **500**, 415–421 (2013).
64. Lai, D., Ha, G., & Shah, S. HMMcopy: Copy number prediction with correction for GC and mappability bias for HTS data. HMMcopy, R package version 1.44.0 <https://doi.org/doi:10.18129/B9.bioc.HMMcopy> (2023).
65. Kwok, A. W. C. et al. MQuad enables clonal substructure discovery using single cell mitochondrial variants. *Nat. Commun.* **13**, 1205 (2022).
66. Butler, A., Hoffman, P., Smibert, P., Papalexi, E. & Satija, R. Integrating single-cell transcriptomic data across different conditions, technologies, and species. *Nat. Biotechnol.* **36**, 411–420 (2018).

67. Stuart, T. et al. Comprehensive integration of single-cell data. *Cell* **177**, 1888–1902 (2019).
68. Zhang, A. W. et al. Probabilistic cell-type assignment of single-cell RNA-seq for tumor microenvironment profiling. *Nat. Methods* **16**, 1007–1015 (2019).
69. Korsunsky, I. et al. Fast, sensitive and accurate integration of single-cell data with Harmony. *Nat. Methods* **16**, 1289–1296 (2019).
70. Pencina, M. J. & D'Agostino, R. B. Overall C as a measure of discrimination in survival analysis: model specific population value and confidence interval estimation. *Stat. Med.* **23**, 2109–2123 (2004).
71. Benedetti, E. et al. A multimodal atlas of tumour metabolism reveals the architecture of gene-metabolite covariation. *Nat. Metab.* **5**, 1029–1044 (2023).
72. Therneau, T. M., Lumley, T., Elizabeth, A. & Cynthia, C. survival: survival analysis. R version 3.2.3. CRAN.R-project.org/package=survival (2022).
73. Kim, M. Single cell mtDNA dynamics in tumors is driven by co-regulation of nuclear and mitochondrial genomes. Zenodo 10.5281/zenodo.10498239 (2024).
74. Kim, M. et al. mtdna dlp. GitHub github.com/reznik-lab/mtdna-dlp (2024).

Acknowledgements

We acknowledge the constructive feedback of the Shah and Reznik Labs. This project was generously supported by the Cycle for Survival, the Marie-Josée and Henry R. Kravis Center for Molecular Oncology and the National Cancer Institute Cancer Center Core (grant P30-CA008748) supporting Memorial Sloan Kettering Cancer Center. S.P.S. holds the Nicholls Biondi Chair in Computational Oncology and is a Susan G. Komen Scholar (GC233085). This work was also funded in part by awards to S.P.S.: Susan G. Komen Breast Cancer Foundation (SAC220206), the Cancer Research UK Grand Challenge Program (GC-243330) and an NIH RM1 award (RM1-HG011014). E.R. was supported by the Department of Defense Kidney Cancer Research Program (W81XWH-18-1-0318 and HT9425-23-1-0995), Cycle For Survival Equinox Innovation Award, Kidney Cancer Association Young

Investigator Award, Brown Performance Group Innovation in Cancer Informatics Fund and NIH (R37 CA276200). E.R. was also supported by a grant from the Alan and Sandra Gerry Metastasis and Tumor Ecosystems Center.

Author contributions

S.P.S., E.R. and S.A. conceived and supervised the study. M.K. led all data analysis. S.P.S., S.A. and C.O. designed and performed the experiments. S.P.S., E.R., S.A. and M.K. designed the statistical model. Additional data analysis was performed by A.G., N.C., T.F., I.V., D.G., S.S., A.C.W., H.S., A.M., T.P., S.B. and H.J. with genomic data collection and analytical methodology development. S.P.S., E.R. and M.K. wrote the manuscript with help from M.W., C.T., N.R. and P.A.G. All authors provided feedback on and approved the paper.

Competing interests

S.P.S. has an advisory role to AstraZeneca. S.A. is a founder and shareholder of GenomeTherapeutics (Inflex) and scientific advisor to Sangamo Therapeutics, Chordia Biosciences and the Institute of Cancer Research, London. All roles are outside the scope of this manuscript. The remaining authors declare no competing interests.

Additional information

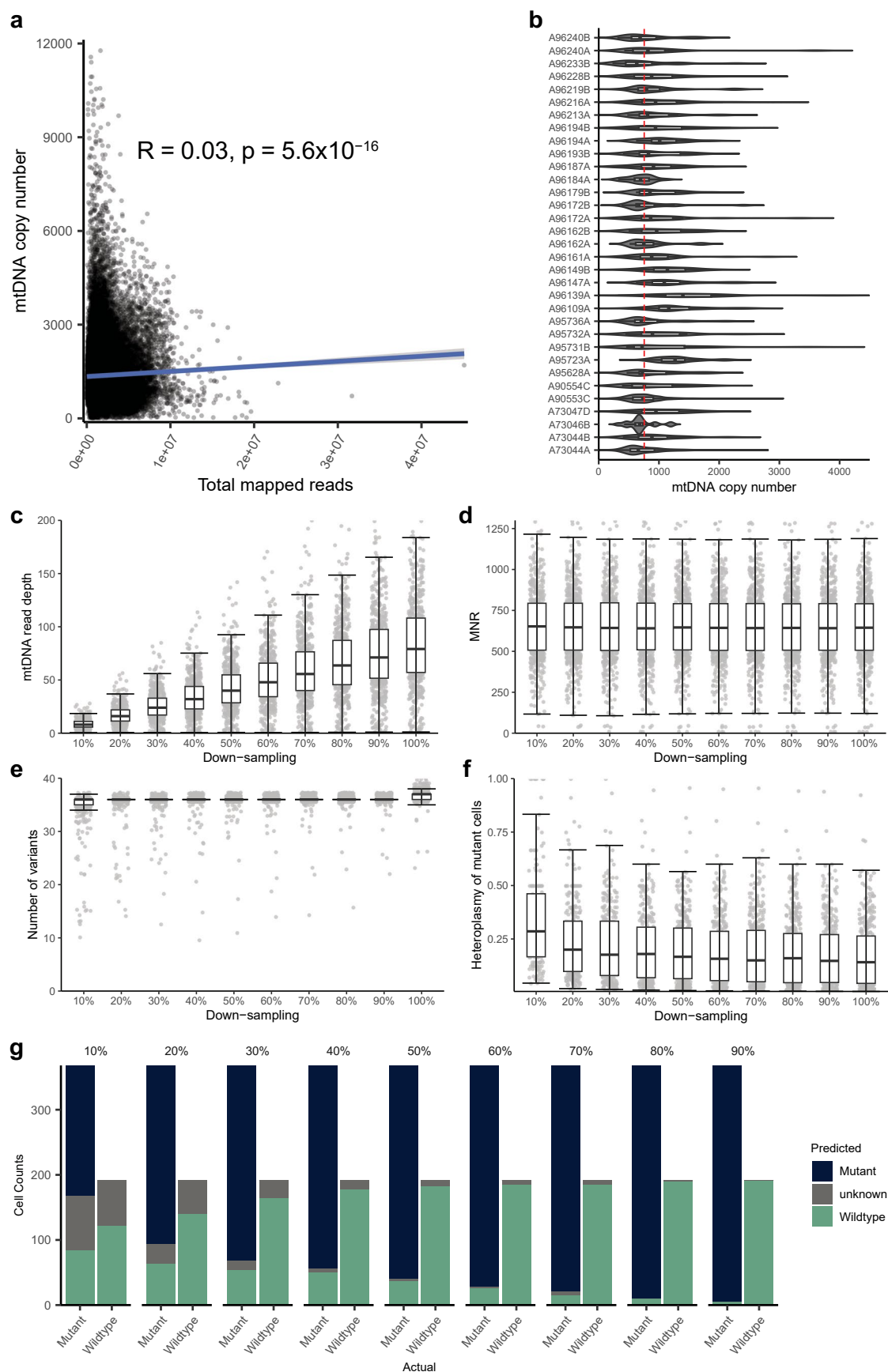
Extended data is available for this paper at
<https://doi.org/10.1038/s41588-024-01724-8>.

Supplementary information The online version contains supplementary material available at <https://doi.org/10.1038/s41588-024-01724-8>.

Correspondence and requests for materials should be addressed to Sohrab P. Shah or Ed Reznik.

Peer review information *Nature Genetics* thanks Konstantin Khrapko, Caleb Lareau, and the other, anonymous, reviewer(s) for their contribution to the peer review of this work.

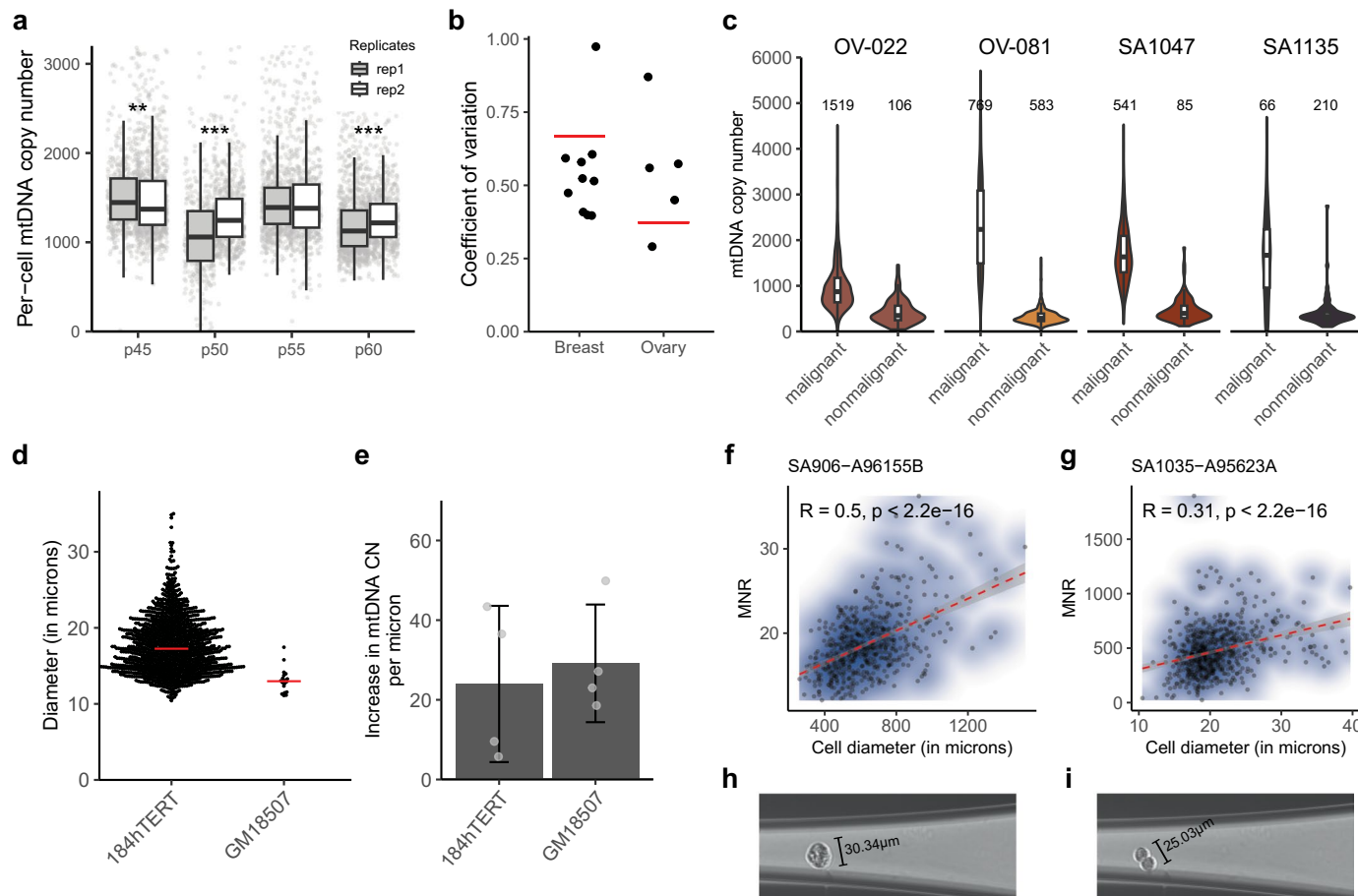
Reprints and permissions information is available at www.nature.com/reprints.



Extended Data Fig. 1 | See next page for caption.

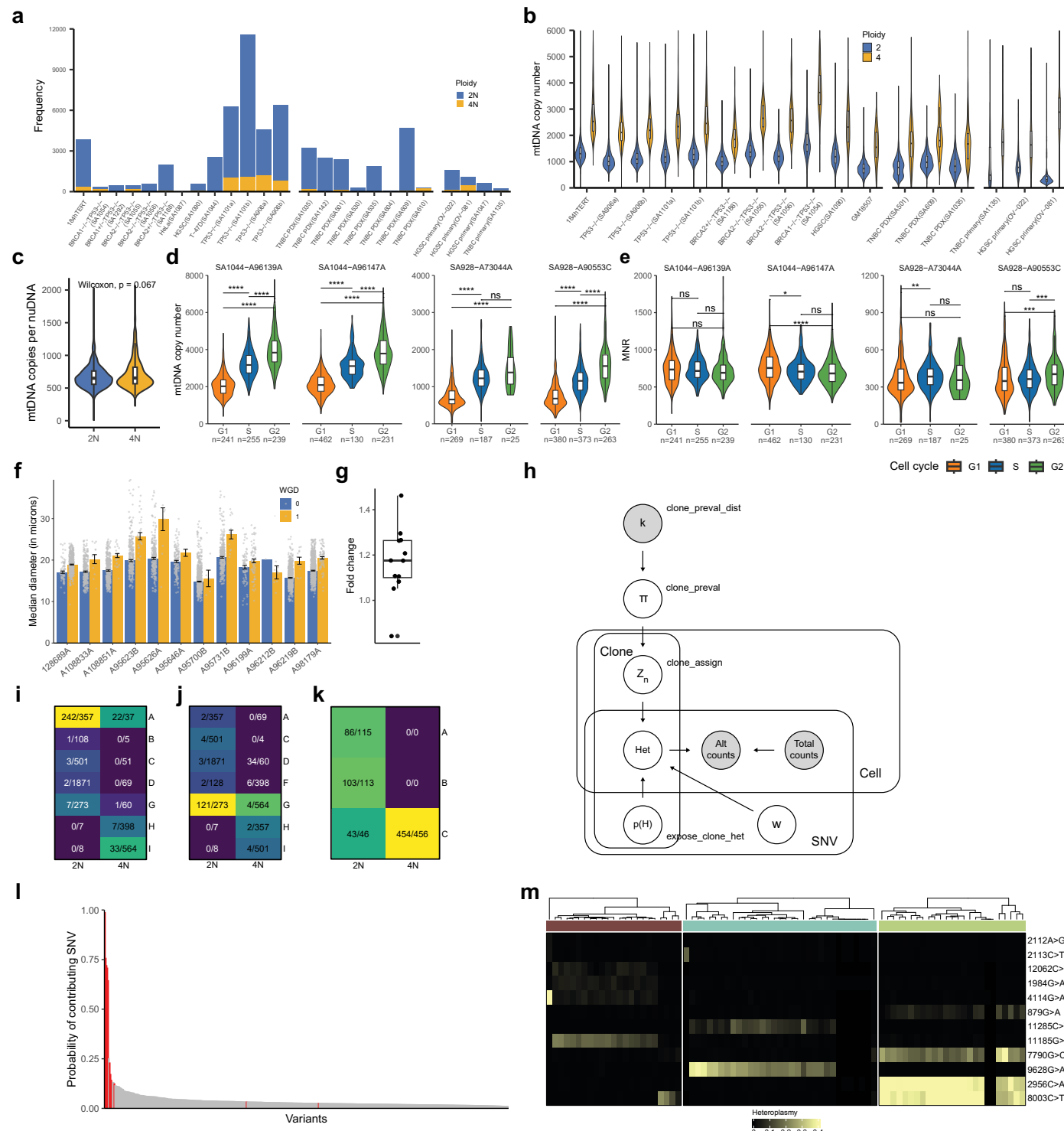
Extended Data Fig. 1 | Robust single-cell quantification of mtDNA copy number based on DLP⁺. **a**, Scatter plot of mtDNA copy number against total mapped read counts for each cell. Two-sided Pearson correlation between mtDNA copy number and total mapped reads results in a correlation coefficient of 0.03, $P < 5.6 \times 10^{-16}$. Gray-shaded areas represent error bands indicating the 95% confidence interval, and the blue line indicates the regression line. **b**, Per-cell mtDNA copy number estimation of GM18507 lymphoblastoid cells across 33 libraries with at least 15 cells ($n = 2,281$). All boxplots represent the median, 25th percentile and 75th percentile, and whiskers correspond to 1.5 times the interquartile range. **c**, Downsampling experiment of a SA1090 (OV2295 cell line) library ($n = 573$ cells) showing a gradual decrease in mtDNA read depth from right to left. All boxplots in the downsampling experiment represent the median, 25th percentile and 75th percentile, and whiskers correspond to 1.5 times the interquartile range. **d**, MNR across all levels of downsampling shows a very consistent MNR around 647 (two-sided, two-sample Wilcoxon test against the original library; all $P > 0.78$). **e**, Boxplot of the number of variants detected across

all levels of downsampling. Total of 37 variants were detected in the original 100% sequencing library. On the other hand, the downsampling resulted in a very stable number of variants at 36 across all levels. The number of variants drastically varied only when the library was down-sampled to 10%. **f**, Distribution of heteroplasmy level of one heteroplasmic variant, m.15500G>A, that was at low heteroplasmy level in the original 100% sequencing depth across all levels of downsampling. The median heteroplasmy was consistent with the original until 30%, below which we saw the median heteroplasmy increase with many cells dropping out. Also, more cells exhibited discrete levels of heteroplasmy due to lower sequencing depth. All boxplots represent the median, 25th percentile and 75th percentile, and whiskers correspond to 1.5 times the interquartile range. **g**, For the same variant, m.15500G>A, the breakdown of the mutant status assignment of the cells with the original 100% sequencing depth is as the ground truth. At 30% of the original sequencing depth, we start to classify true mutant cells as wild-type cells with sensitivity of 0.85 and specificity of 1.



Extended Data Fig. 2 | mtDNA copy number represents biophysical and genomic cellular energy demand. **a**, Boxplots showing the distribution of mtDNA copy number across technical replicates over four different time points. *P*-values from the two-sided, two-sample Wilcoxon test are indicated above. The boxplot represents the median, 25th percentile and 75th percentile, and whiskers correspond to 1.5 times the interquartile range. ** denotes $P < 0.01$, *** denotes $P \leq 0.001$ and no annotation denotes $P > 0.1$. **b**, Coefficient of variation in mtDNA copy number across cells in TNBC ($n = 10$) and HGSC ($n = 5$) samples. Red lines indicate a coefficient of variation across breast and ovary bulk tissue tumor samples in PCAWG. **c**, Violin plot of the per-cell mtDNA copy number across malignant and nonmalignant cells across four primary tumors with sufficiently high nonmalignant cells (OV-022: $n = 1,625$ cells, OV-081: $n = 1,352$ cells, SA1047: $n = 626$ cells, SA1135: $n = 276$ cells, all $P < 10^{-16}$). Two-sided, two-sample Wilcoxon test indicates that malignant cells have a significantly higher mtDNA copy number compared to nonmalignant cells across all four tumor samples. The boxplot represents the median, 25th percentile and 75th percentile, and whiskers

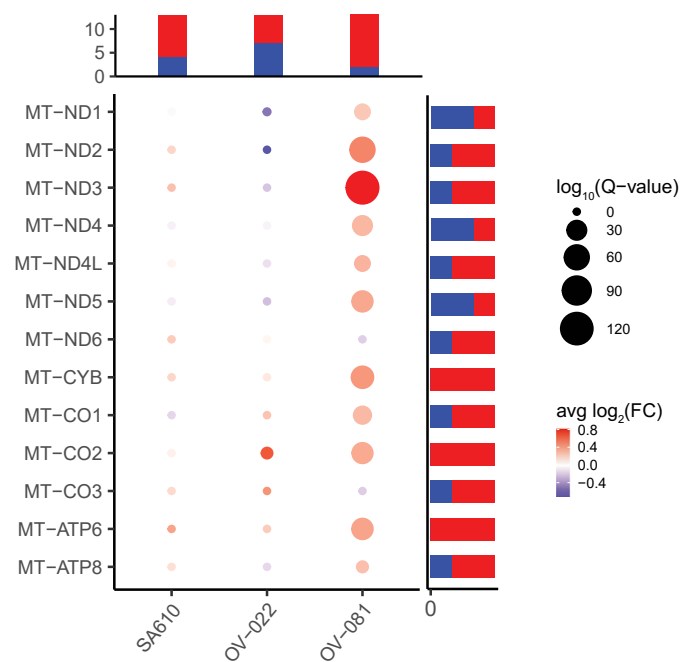
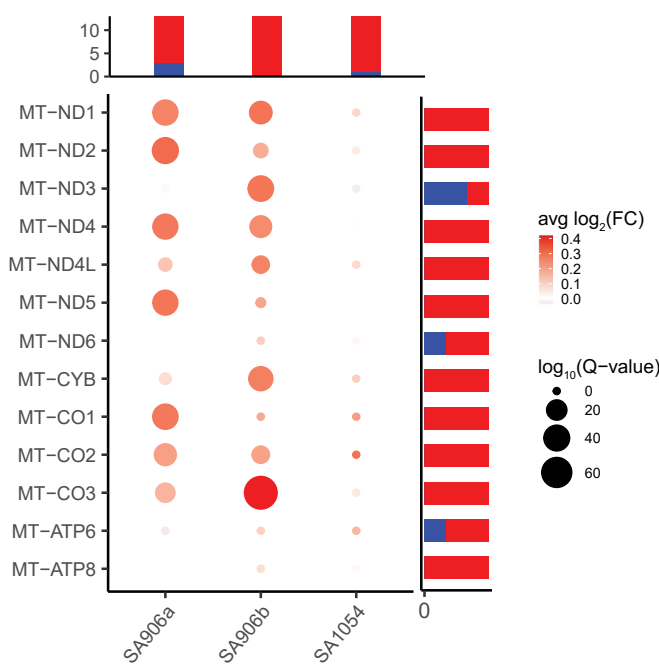
correspond to 1.5 times the interquartile range. **d**, Distributions of cell diameter in microns for GM18507 ($n = 18$ cells) and 184-hTERT diploid cells ($n = 1,152$ cells). **e**, Coefficient for the diameter term in the linear regression model of mtDNA copy number against cell diameter for diploid 184-hTERT and GM18507 cells only ($n = 4$ libraries each). Error bars represent SD of the coefficient values. **f**, A scatter plot showing a positive two-sided Pearson correlation between MNR and cell diameter for a sequencing library of a TP53^{-/-} 184-hTERT SA906b cell line, A96155B. Gray-shaded areas represent error bands indicating the 95% confidence interval, and the red dotted line indicates the regression line. **g**, Same as **f** but for a sequencing library of a TNBC SA1035 PDX, A95623A. **h**, Microscopic image of a true tetraploid cell from a TP53^{-/-} 184-hTERT breast epithelial cell library, SA906-A96228B, taken during cell dispensing as part of the DLP+. The cell size is slightly larger than diploid cells in the same library. **i**, Microscopic image of a doublet from the same library. Although the ploidy is estimated as tetraploid, there are actually two diploid cells sequenced together.



Extended Data Fig. 3 | See next page for caption.

Extended Data Fig. 3 | Within-clone analysis of mtDNA-nuDNA ratio in response to whole-genome doubling. **a**, Total number and proportion of diploid and tetraploid cells plotted for each sample. **b**, Comparison of mtDNA copy number between diploid and tetraploid cells across all 9 184-hTERT cell lines and 7 tumor samples as well as GM18507 lymphoblastoid cells (two-sided, two-sample Wilcoxon test, all $P < 7.7 \times 10^{-9}$). All boxplots represent the median, 25th percentile and 75th percentile, and whiskers correspond to 1.5 times the interquartile range. **c**, Violin plot of MNR in diploid ($n = 3,475$) and tetraploid ($n = 350$) cells across all four 184-hTERT breast epithelial cell lines. There is no significant difference between the two groups (two-sided, two-sample Wilcoxon test, $P = 0.067$). All boxplots represent the median, 25th percentile and 75th percentile, and whiskers correspond to 1.5 times the interquartile range. **d**, Boxplot of the mtDNA copy number distribution of cell cycle-sorted cells in different phases, G1, S and G2, across two sequencing libraries of T-47D breast cancer cell line, SA1044-A96139A ($n = 735$ cells) and SA1044-A96147A ($n = 823$ cells) and of lymphoblastoid cell line, SA928-73044A ($n = 481$ cells) and SA928-A90553C ($n = 1,016$ cells). All boxplots represent the median, 25th percentile and 75th percentile, and whiskers correspond to 1.5 times the interquartile range. Pairwise significance is indicated by two-sided Wilcoxon tests. **e**, Same as **d**, but for MNR. **f**, Bar plot of the median diameter, measured in microns, for both

diploid and tetraploid cells for each library across the 12 sequencing libraries of tumor samples. **g**, Boxplot of the median, 25th percentile and 75th percentile of fold change of median diameter for tetraploid cells over diploid cells across the same 12 sequencing libraries in **f**. The whiskers correspond to 1.5 times the interquartile range. **h**, Graphical model of MityBayes. MityBayes takes raw counts of the alternate allele and total depth per cell across mtDNA variants. It infers the clonal assignment of the cells based on clone-specific heteroplasmy level and weighing of informative variants. **i**, Heatmap indicating the presence of mtDNA variant, m.1429C>T. Each cell indicates a fraction of mutant cells out of the total number of cells corresponding to diploid and tetraploid across clones in *TP53^{-/-}* 184-hTERT sample, SA906a. This variant is present in both diploid and tetraploid cells of clone A. **j**, Same as **i** but for m.6869C>T in *TP53^{-/-}* 184-hTERT sample, SA906a. This variant is present in both diploid and tetraploid cells of clone G. **k**, Same as **i** but for m.6708G>A in SPECTRUM-OV-081 sample. This variant is present in both diploid and tetraploid cells of clone C. **l**, Ranking of the weight variable that indicates the probability of the variant contributing to the clonal assignment is plotted in a descending order. The real variants were colored in red. **m**, Heatmap of heteroplasmy across clones determined from mtDNA variants. The mtDNA variants-based clonal labels are on the top.

a**b**

Extended Data Fig. 4 | Transcriptional phenotype of high MNR cells compared against low MNR cells in tumors. **a**, Differential expression of mtDNA-encoded genes between clones with the highest and lowest MNR

across the tumor samples based on Wilcoxon rank sum test. Colors indicate the average log₂ fold change, while the dot size indicates the log₁₀ of adjusted p-values. **b**, Same as **a** but for engineered 184-hTERT cell lines.

Reporting Summary

Nature Portfolio wishes to improve the reproducibility of the work that we publish. This form provides structure for consistency and transparency in reporting. For further information on Nature Portfolio policies, see our [Editorial Policies](#) and the [Editorial Policy Checklist](#).

Statistics

For all statistical analyses, confirm that the following items are present in the figure legend, table legend, main text, or Methods section.

n/a Confirmed

- The exact sample size (n) for each experimental group/condition, given as a discrete number and unit of measurement
- A statement on whether measurements were taken from distinct samples or whether the same sample was measured repeatedly
- The statistical test(s) used AND whether they are one- or two-sided
Only common tests should be described solely by name; describe more complex techniques in the Methods section.
- A description of all covariates tested
- A description of any assumptions or corrections, such as tests of normality and adjustment for multiple comparisons
- A full description of the statistical parameters including central tendency (e.g. means) or other basic estimates (e.g. regression coefficient) AND variation (e.g. standard deviation) or associated estimates of uncertainty (e.g. confidence intervals)
- For null hypothesis testing, the test statistic (e.g. F , t , r) with confidence intervals, effect sizes, degrees of freedom and P value noted
Give P values as exact values whenever suitable.
- For Bayesian analysis, information on the choice of priors and Markov chain Monte Carlo settings
- For hierarchical and complex designs, identification of the appropriate level for tests and full reporting of outcomes
- Estimates of effect sizes (e.g. Cohen's d , Pearson's r), indicating how they were calculated

Our web collection on [statistics for biologists](#) contains articles on many of the points above.

Software and code

Policy information about [availability of computer code](#)

Data collection All commercial, open source and custom code software is detailed in the Methods section.

Data analysis Mutect2 (GATK v4.1.2.0), Samtools (v1.9), CellRanger software (v4.0.0), cellassign (v0.99.2), and CloneAlign (v0.99.0)
R packages: R (v4.2.3), Seurat R package (v3.0.1), Harmony (v0.1).

Custom software that is part of this study is available as specified in the Methods section: R code to regenerate all figures is available on Github (<https://github.com/reznik-lab/mtdna-dlp>) with the relevant data and instructions to execute the code.

For manuscripts utilizing custom algorithms or software that are central to the research but not yet described in published literature, software must be made available to editors and reviewers. We strongly encourage code deposition in a community repository (e.g. GitHub). See the Nature Portfolio [guidelines for submitting code & software](#) for further information.

Data

Policy information about [availability of data](#)

All manuscripts must include a [data availability statement](#). This statement should provide the following information, where applicable:

- Accession codes, unique identifiers, or web links for publicly available datasets
- A description of any restrictions on data availability
- For clinical datasets or third party data, please ensure that the statement adheres to our [policy](#)

The DLP+ and scRNA-seq data associated with the study spans already publicly available datasets from European Genome-Phenome archive and dbGaP:

- DLP+ data from Laks et al. 2019 is available from EGAS00001006343
- DLP+ data from Salehi et al. 2021 is available from EGAS00001004448
- DLP+ and scRNA-seq data from Funnell et al. 2022 is available from EGAS00001003190
- The MSK SPECTRUM dataset is available via dbGaP (accession number phs002857.v2.p1: http://www.ncbi.nlm.nih.gov/projects/gap/cgi-bin/study.cgi?study_id=phs002857.v2.p1)

The reference file:

- Pre-built reference GRCh38 transcriptome (version 3.0.0) is available from 10x Genomics

The processed data are available on Zenodo (<https://zenodo.org/records/10498240>)

Research involving human participants, their data, or biological material

Policy information about studies with [human participants or human data](#). See also policy information about [sex, gender \(identity/presentation\), and sexual orientation](#) and [race, ethnicity and racism](#).

Reporting on sex and gender

N/A

Reporting on race, ethnicity, or other socially relevant groupings

N/A

Population characteristics

N/A

Recruitment

N/A

Ethics oversight

N/A

Note that full information on the approval of the study protocol must also be provided in the manuscript.

Field-specific reporting

Please select the one below that is the best fit for your research. If you are not sure, read the appropriate sections before making your selection.

Life sciences

Behavioural & social sciences

Ecological, evolutionary & environmental sciences

For a reference copy of the document with all sections, see nature.com/documents/nr-reporting-summary-flat.pdf

Life sciences study design

All studies must disclose on these points even when the disclosure is negative.

Sample size

Cell lines and PDX cohort:

For each time series sample, we estimated power to detect clones to 2% for choosing the number of cells to sequence. For number of samples per time series, this was determined due to practical constraints, sampling tumours over a 2.5yr interval. No calculations were used to determine the number of samples/time series.

Quality-filtered study datasets (MSK SPECTRUM cohort):

- scRNA-seq: 2 patients, 5 samples, 2,977 cells

Data exclusions

For all samples, low quality sequenced cells and cells with very few reads mapping to mtDNA were excluded.

Replication

Replicates were performed in the cell lines and the TNBC-SA609 Line 1 Untreated PDX, via one and two 'mixing' experiment respectively to reproduce the observation of fitness clones.

Patients with multi-site data had 2-3 samples profiled by DLP+.

Randomization

Randomization was not applicable in this study because the cell line experiments were controlled perturbation experiments, generating time series with or without isogenic TP53 mutation.

Reporting for specific materials, systems and methods

We require information from authors about some types of materials, experimental systems and methods used in many studies. Here, indicate whether each material, system or method listed is relevant to your study. If you are not sure if a list item applies to your research, read the appropriate section before selecting a response.

Materials & experimental systems

n/a	Involved in the study <input checked="" type="checkbox"/> Antibodies <input type="checkbox"/> Eukaryotic cell lines <input checked="" type="checkbox"/> Palaeontology and archaeology <input type="checkbox"/> Animals and other organisms <input checked="" type="checkbox"/> Clinical data <input checked="" type="checkbox"/> Dual use research of concern <input checked="" type="checkbox"/> Plants
-----	---

Methods

n/a	Involved in the study <input checked="" type="checkbox"/> ChIP-seq <input checked="" type="checkbox"/> Flow cytometry <input checked="" type="checkbox"/> MRI-based neuroimaging
-----	---

Eukaryotic cell lines

Policy information about [cell lines and Sex and Gender in Research](#)

Cell line source(s)

Cell lines were generated from the commercially available 184-hTERT cell line as previously described (references [1-4]) and as indicated in the Methods section: "the samples include (1) an immortalized normal human female breast epithelial cell line 184-hTERT L9, (2) four sets of 184-hTERT cell lines with perturbation in TP53-/ passaged over multiple timepoints, (3) five 184-hTERT cell lines with a variety of genetic perturbations in the repair pathway, including TP53-/, BRCA1-/, BRCA2+/- and BRCA2-/-,..., and (5) GM18507 lymphoblastoid cell line."

Authentication

These cell lines were used previously and reported in previous papers from our laboratory:
 1. Laks, E. et al. Clonal Decomposition and DNA Replication States Defined by Scaled Single-Cell Genome Sequencing. *Cell* 179, 1207–1221 (2019).
 2. Salehi, S. et al. Clonal fitness inferred from time-series modelling of single-cell cancer genomes. *Nature* 595, 585–590 (2021).
 3. Funnell, T. et al. Single-cell genomic variation induced by mutational processes in cancer. *Nature* (2022) doi:10.1038/s41586-022-05249-0.

Mycoplasma contamination

Mycoplasma testing was negative.

Commonly misidentified lines (See [ICLAC](#) register)

No commonly misidentified cell lines were used in the study.

Animals and other research organisms

Policy information about [studies involving animals; ARRIVE guidelines](#) recommended for reporting animal research, and [Sex and Gender in Research](#)

Laboratory animals

The details on mouse strains for xenografting tumours can be found in Section 2 of the Supplementary Information of a previous paper from our laboratory
 Reference [1]

Wild animals

These PDX models were reported in previous papers from our laboratory:
 1. Salehi, S. et al. Clonal fitness inferred from time-series modelling of single-cell cancer genomes. *Nature* 595, 585–590 (2021).

Reporting on sex

Indicate if findings apply to only one sex; describe whether sex was considered in study design, methods used for assigning sex. Provide data disaggregated for sex where this information has been collected in the source data as appropriate; provide overall numbers in this Reporting Summary. Please state if this information has not been collected. Report sex-based analyses where performed, justify reasons for lack of sex-based analysis.

Field-collected samples

For laboratory work with field-collected samples, describe all relevant parameters such as housing, maintenance, temperature, photoperiod and end-of-experiment protocol OR state that the study did not involve samples collected from the field.

Ethics oversight

The Ethics Committees at the University of British Columbia approved all the experiments using human resources. Patients in Vancouver, British Columbia were recruited, and samples were collected under the tumour tissue repository (TTRH06-00289) protocol and transplanted in mice under the Neoadjuvant PDX (University of British Columbia BC Cancer Research Ethics Board H20-00170) protocols.

After informed consent, tumour fragments from patients undergoing excision or diagnostic core biopsy were collected. Tumour

materials were processed and transplanted in mice under the animal resource centre (ARC) bioethics protocol (A19-0298-A001) approved by the animal care committee.

Note that full information on the approval of the study protocol must also be provided in the manuscript.